2019-07-01

Nature and Origin of Fissure Ore at the Porphyry-Epithermal Transition Zone of the Bingham Canyon Porphyry Cu-Au-Mo Deposit, Utah

David Harris Tomlinson
Brigham Young University

Follow this and additional works at: https://scholarsarchive.byu.edu/etd

Nature and Origin of Fissure Ore at the Porphyry-Epithermal Transition Zone

of the Bingham Canyon Porphyry Cu-Au-Mo Deposit, Utah

David Harris Tomlinson Jr.

A thesis submitted to the faculty of
Brigham Young University
in partial fulfillment of the requirements for the degree of

Master of Science

Eric H. Christiansen, Chair
Michael John Dorais
Jeffrey D. Keith

Department of Geological Sciences

Brigham Young University

ABSTRACT

Nature and Origin of Fissure Ore at the Porphyry-Epithermal Transition Zone
of the Bingham Canyon Porphyry Cu-Au-Mo Deposit, Utah

David Harris Tomlinson Jr.
Department of Geological Sciences, BYU
Master of Science

Late-stage fissure-filling ore at the world class Bingham Canyon, Utah, porphyry copper deposit has long been recognized, but poorly studied. Physical and chemical characterization of the Pb-Zn-Cu-Ag-Au mineralized fissures in the porphyry-epithermal transition zone provides insight into the origin, timing, and controls of ore deposition. These sheared sulfide-rich fissures are dominated by pyrite and multiple generations of quartz, with lesser amounts of other sulfides and gangue minerals. Au (0.27 to 4.61 ppm) provides the most value to the ore in the transition zone. Host rocks include Eocene monzonite and Paleozoic limestone and quartzite—all of which can contain economic ore bodies. Associated alteration is predominantly sericitic and argillic. Mineralization into the wall rocks is restricted, not exceeding 1.5 m from the fissure margins. Mineral assemblages vary with distance from the center of the main Cu-Mo deposit and the modal abundances are dependent on host rock. The appearance of both galena and sphalerite (and tennantite to an extent) mark the transition from a porphyry to an epithermal environment. This is accompanied by an increased concentration of chalcophile trace elements in sulfides as determined by EMPA and LA-ICP-MS. Significant hosts of Ag include galena and tennantite, while Cu is hosted primarily in chalcopyrite, tennantite, and sphalerite. Gold does not appear to be hosted in solid solution, but may be focused along fractures or inclusions in pyrite. $\delta^{34}S$ values of fissure pyrite has a narrow range (+2.3 to 3.4‰), while $\delta^{18}O$ of quartz is more variable and high (+11.5 to 14.0‰) relative to typical hydrothermal quartz. This can be explained by increased fractionation at lower temperatures in the magmatic fluids, which could have additionally mixed with exchanged ^{18}O-rich meteoric water. Ore grades improve with distance from the center of the deposit; however, this is accompanied by higher concentrations of elements (Pb, As, Bi, etc.) undesirable for downstream processing. The mineralized fissures were created sequentially throughout the formation of the deposit. Initial joints probably formed as a result of the intrusion of a barren equigranular monzonite. The NE orientation of the joints was controlled by the regional stress field, which is more apparent distal to the center of the deposit. A quartz monzonite porphyry then intruded, dilating the joints to allow precipitation of quartz and then pyrite during the Cu-Au-stage of mineralization in the main ore body. After dike-like intrusions of latite porphyry and quartz latite porphyry intruded, galena, sphalerite, and pyrite precipitated to form the Pb-Zn-Ag mineralization. This was followed by late precipitation of chalcopyrite and tennantite (and likely Au mineralization).

Keywords: Bingham, porphyry copper, gold, fissure, base metal, Utah, vein, epithermal, LA-ICP-MS, transition

ACKNOWLEDGEMENTS

This project would have never come to fruition without the help of several individuals and organizations. I would like to initially thank my committee chair, Dr. Eric H. Christiansen, for his support and trust in allowing me to select a project in something I was truly passionate about. His guidance, suggestions, and discussion helped shape this project from an idea to a valuable contribution in economic geology. I am also grateful for my committee members, Dr. Jeffrey Keith and Dr. Michael Dorais, for their valuable discussion and feedback, and their help in data acquisition. I cannot forget to thank Alec Martin who saved me weeks of work in both sample preparation and data reduction, which allowed me to be far more effective as a student.

I would also like to acknowledge Rio Tinto, their geologists, and engineers for their time, resources, and permission to do this project. Specifically, I would like to thank Rudy Ganske, Mackenzie Sorenson, Nick Vetz, Stan Nelson, Jennifer Baar, Kathleen Gundy, Jens Gibbs, Kim Schroeder, Craig McClung, and Ksenia Kashina for their valuable input and contribution.

The Society of Economic Geologists is thanked for the research funds they provided in the form of a Graduate Student Fellowship. Their crucial contribution allowed this project to go into greater depths than would have been possible initially.

Most importantly, I would like to thank my family for their support, patience, and love as I worked through this project. They had to put a lot on hold for me to finish my degree, and I hope I can offer the same support in return for their future aspirations. My wife put many more hours supporting me through this project then it took to complete it, and I am indebted to her for all her help.

TABLE OF CONTENTS

LIST OF TABLES

LIST OF FIGURES

INTRODUCTION

The Bingham Canyon mine is developed in a porphyry Cu-Au-Mo deposit in the

OquirrhMountains of northern Utah and centered on an Eocene igneous complex. It has been in

operation for more than 115 years and produced over 19 million tons of copper as well as

substantial amounts of gold, silver, molybdenum, and sulfuric acid (www.kennecott.com,

accessed March 2018). Apart from the deposit's massive size, it is also unique because it

contains all of the ore types associated with porphyry Cu systems including: a porphyry Cu-Au-

Mo deposit, Cu-Au skarns, carbonate-replacement Zn-Pb-Ag-Au, Pb-Zn-Cu-Ag-Au veins, and

sediment-hosted Au deposits (Sillitoe, 2010).

The mine is currently expanding its open-pit operations in an attempt to reach deeper

reserves along the southern flank of the pit. During this expansion, mineralized fissures have

been reencountered. The term "fissure" in this and past studies at Bingham refers to large (cm to

m scale), sulfide-rich veins, which often show evidence of shear during late faulting. They form

ore bodies that vary greatly in size, grade, and geometry even on a single 15 m mine bench,

which complicates production predictions. Extensive underground mining exploited these

fissures on the southern edge of the deposit for Pb, Zn, and Ag as far back as the late 1800s.

Today, advancements in open-pit mining techniques and downstream processing have allowed

this fissure ore to be economic at Bingham. Rather than being mined for Pb, Zn, and Ag, this ore

is currently being mined to supplement the production of Cu, Au, and Ag, of which Au

contributes the most overall value. This has sparked a renewed interest in further understanding

these mineralized fissures and their origin.

Porphyry-related base metal veins, like the fissures in this study, have been referred to as

the deeper counterparts of shallow intermediate-sulfidation epithermal veins (Sillitoe, 2010).

Intermediate- to high-sulfidation epithermal deposits are often considered shallow components of

porphyry Cu systems (Einaudi et al., 2003) linked by a "transition" zone (Maydagán et al., 2013)(Fig. 1). In this transition zone, epithermal-style mineralization can overprint porphyry-style mineralization evidenced by physical textures and chemical composition of sulfides (Sykora et al., 2018). These late-stage porphyry-related veins show well-developed zoning both spatially and temporally with increased Pb-Zn-Ag mineralization towards the outer fringes and late Cu-Fe sulfides and sulfosalts (Einaudi et al., 2003).

There have been some studies that have incorporated the Bingham fissures (Boutwell, 1905; James et al., 1961; Field, 1966; Field and Moore, 1971; Atkinson and Einaudi, 1978). However, many of these are restricted to the base metal mineralization associated with the fissures beyond active mining operations or in areas where the material has since been removed. This study expands on previous work in order to characterize the fissures from a macro to micro scale at the current levels of mining. In addition, we determine possible origins, timing, and controls of mineralization by studying their physical and chemical nature as it correlates with distance to the center of the deposit.

REGIONAL GEOLOGIC SETTING

The Bingham deposit is located in northern Utah along the eastern flank of the Oquirrh Mountains and is regionally aligned with other Eocene ore-related stocks. The basement rock consists of Paleoproterozoic paragneiss and orthogneiss of the Mojave province, which was metamorphosed 1.8-1.7 Ga (Yonkee and Weil, 2015). Metamorphism was the result of the accretion of the Yavapai Province during the early assembly of North America (Whitmeyer and Karlstrom, 2007). Arc accretion, granitoid intrusion, and orogenisis associated with the assembly of Rodinia continued until 1.1 Ga followed by rifting during its subsequent breakup in the late Proterozoic (Whitmeyer and Karlstrom, 2007). Accumulation of wedge sediment on the subsiding margin in the Pennsylvanian resulted in the formation of the Oquirrh basin in NW
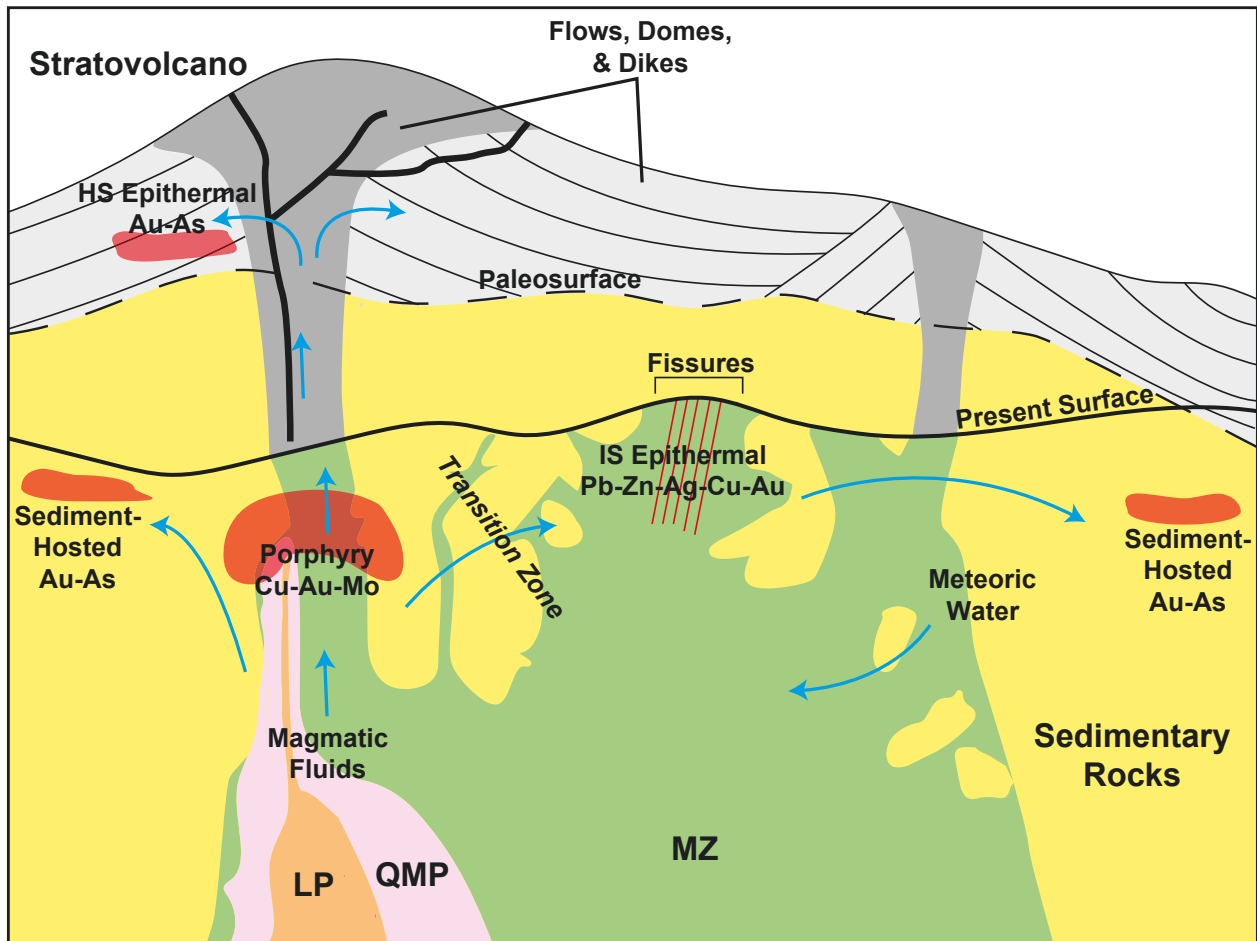
Fig. 1. Simplified cross section of the Bingham porphyry copper system modified from Deino and Keith (1997). Blue arrows indicate fluid pathways, and red shapes and lines represent various deposits within the system. This study is focused on fissure mineralization at "transition zone" between the porphyry and intermediate-sulfidation epithermal environments. MZ-monzonite, QMP-quartz monzonite porphyry, LP-latite porphyry, IS-intermediate-sulfidation, HS-high-sulfidation.

3

Utah and the deposition of thick marine sediment (Yonkee and Weil, 2015), which are locally represented by the Butterfield Peaks Formation and the Bingham Mine Formation (Fig. 2). The onset of subduction drove the Sevier orogeny deforming these sedimentary rocks, which created the large folds within the deposit and the Midas thrust on the northern end of the deposit (Kloppenburg et al., 2010). The sedimentary formations at Bingham consist of dominantly thick arkosic orthoquartzites with some siltstones and limestones (Porter et al., 2012). The Jordan and Commercial limestones represent the base of the Bingham Mine Formation and host high-grade skarns near the contact with the Eocene Bingham intrusive suite (Fig. 2).

The mineralized intrusions can be related to slab roll-back magmatism, which occurred as a result of a progressively steepening dip angle of the subducting Farallon plate during the late-Eocene to early-Oligocene (Best et al., 2016). The series of intrusions were emplaced by horizontal dilation from northwest- and northeast-trending faults (Kloppenburg et al., 2010). These faults have been related to either extension (Presnell, 1997) or thrusting (McKean et al., 2011) towards the end of the Sevier orogeny; they may also be related to the emplacement of the intrusions themselves.

Recent high-precision U-Pb CA-ID-TIMS zircon analyses indicate the ages of the intrusive rocks span from 38.53-37.70 Ma (Large, 2018); these ages are in agreement with those derived from ^{40}Ar/^{39}Ar chronology by Deino and Keith (1997). The relative timing of the intrusions at the Bingham deposit is well established to be from oldest to youngest: equigranular monzonite (38.53 Ma), quartz monzonite porphyry (38.28 Ma), latite porphyry (38.13 Ma), and quartz latite porphyry (37.70 Ma) (Porter et al., 2012; Large, 2018) (Fig. 2). The porphyritic quartz monzonite (Ohio Copper Dike) and hybrid unit have not been adequately dated, but cross-
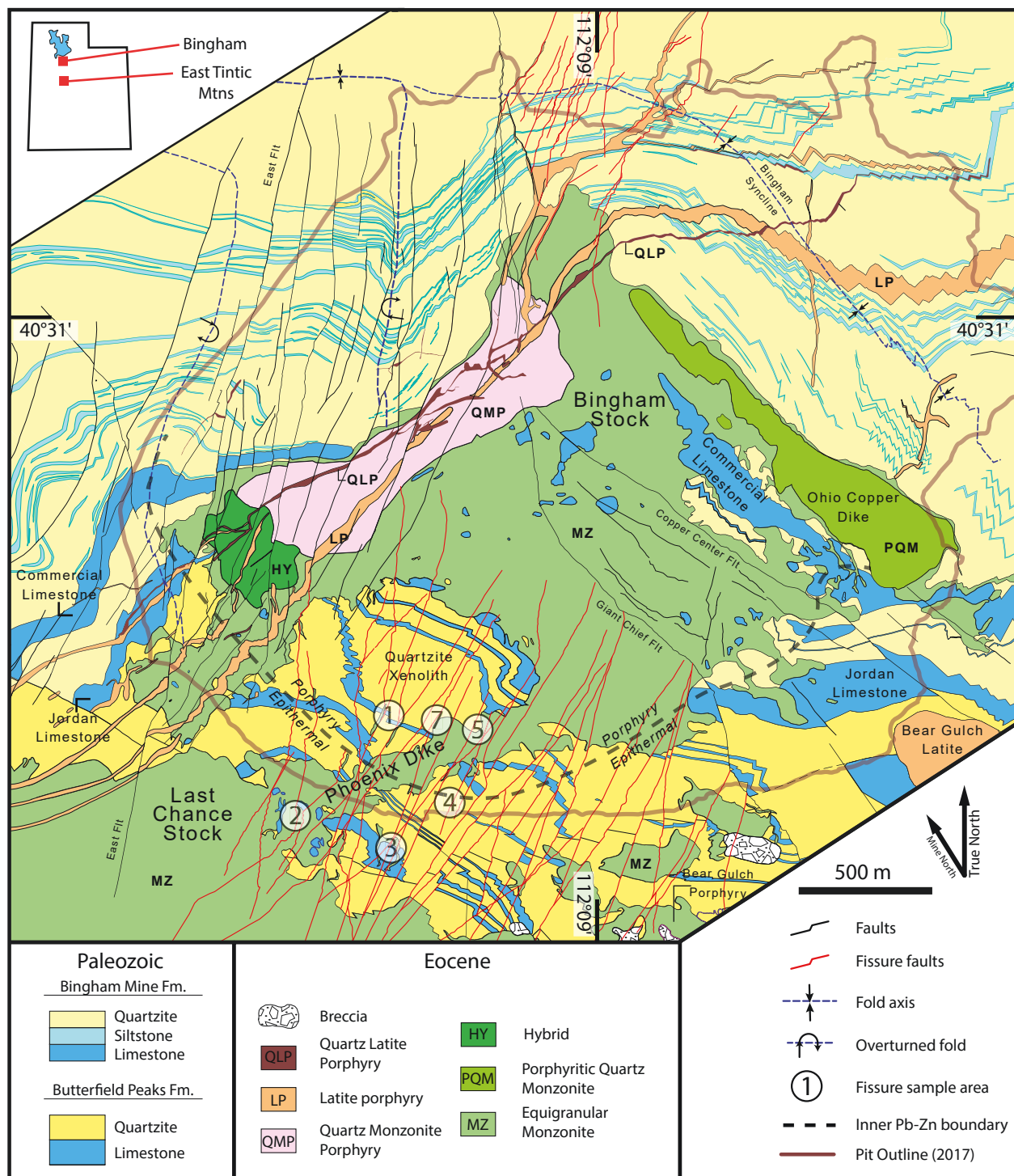
Fig. 2. Geologic map of the Bingham Canyon mine in northern Utah oriented to true north. This study is focused in the SW portion of the mine where NE-trending, late-stage, mineralized fissures (red) are most abundant. The black dashed line indicates where galena and sphalerite mineralization first appear in fissures, which also represents the porphyry-epithermal boundary. Numbers show where samples were taken. In the tables, sample names all begin with prefix "FF". Modified from Porter et al. (2012) with updates provided by mine geologists.

5

cutting relationships suggest they were emplaced soon after the equigranular monzonite and before the quartz monzonite porphyry (Porter et al., 2012).

Co-genetic volcanic rocks just south of the intrusions have allowed a reconstruction of the paleosurface onto which these rocks were deposited to just 500 m above the top of the equigranular monzonite (Deino and Keith, 1997). It has been suggested that shallow intrusions, such as those exposed at the Bingham Canyon mine, simply act as conduits for magmatic fluid from a deeper and larger magmatic source (Sillitoe, 2010). There is no surface exposure of this deeper intrusion, although aeromagnetic and gravity data require that a large batholith underlies the mine at a depth of 2 to 3.5 km with a volume of 1,400 to 3,000 km^3 (Steinberger et al., 2013). Magma mixing involving a large volume of intermediate calc-alkaline magma with lesser amounts of mafic alkaline magma undoubtedly contributed to the metal and sulfur supply of the deposit (Hattori and Keith, 2001; Maughan et al., 2002).

Mineralization at the Bingham deposit follows the conventional porphyry Cu deposit model of a high-grade center with a Cu-barren core—both of which are associated with a potassic alteration zone. The timing of the main mineralizing event has been placed in between the quartz monzonite porphyry and the latite porphyry based on vein cross-cutting relationships (Redmond and Einaudi, 2010). Large (2018) concluded that hydrothermal activity and mineralization occurred in pulses for more than 521 Ky based on the ages of the quartz monzonite porphyry and the quartz latite porphyry and the mineralization linked to each of the intrusions. The ore body is zoned in terms of Cu-Au and Mo mineralization both spatially and temporally (Landtwing et al., 2010). Seo et al. (2012) suggest a change in fluid chemistry over time with early Cu-Au-stage fluids being relatively oxidized and neutral, and late Mo-stage fluids being more reduced and acidic. However, there is general agreement that fluid temperature

was the primary controlling factor for the overall zonation of the mineralization (Landtwing et al., 2005; Redmond and Einaudi, 2010; Sillitoe, 2010).

Temperature gradients are also important controls on the hydrothermal alteration and zonation at Bingham and other porphyry Cu deposits (Sillitoe, 2010). At the Bingham deposit, this includes a potassic center encircled by a large halo of transition to propylitic alteration with vein- and fracture-controlled sericitic and argillic alteration (Bowman et al., 1987; Porter et al., 2012). Bowman et al. (1987) claim sericitic alteration crosscuts both the potassic and propylitic alteration indicating it is late-stage.

LOCAL GEOLOGIC SETTING

Our study is focused in the SW side of the Bingham deposit (Fig. 2), where the dominant ore-related structures are mineralized fissures hosted in units of the equigranular monzonite (Last Chance stock, Phoenix dike, Bear Gulch porphyry, and Bingham stock), and the deformed sedimentary rocks of the Pennsylvanian Butterfield Peaks Formation (primarily quartzite, with lesser amounts of limestone and siltstone). A large block of the Butterfield Peaks Formation (which may be a roof pendant) has been completely enclosed by monzonite with steep, irregular bedding in the sedimentary rocks and is referred to as the "Quartzite Xenolith (Fig. 2)."

The fissures are steep with an average dip of 77° and dip directions ranging from 290-330° and 085-150° true north yielding a dominant NE-SW strike (Fig. 3) This parallels the fissures in the East Tintic mining district (Hildreth and Hannah, 1996). Joints and faults with similar orientations to the fissures have been mapped on the NE side of the deposit (Fig. 2); they are typically only mineralized within the main ore body and they are not as long or continuous as those on the south side. This may be related to structural complications with the Bingham syncline, as there are more bedding-plane faults than fissures on the north side.
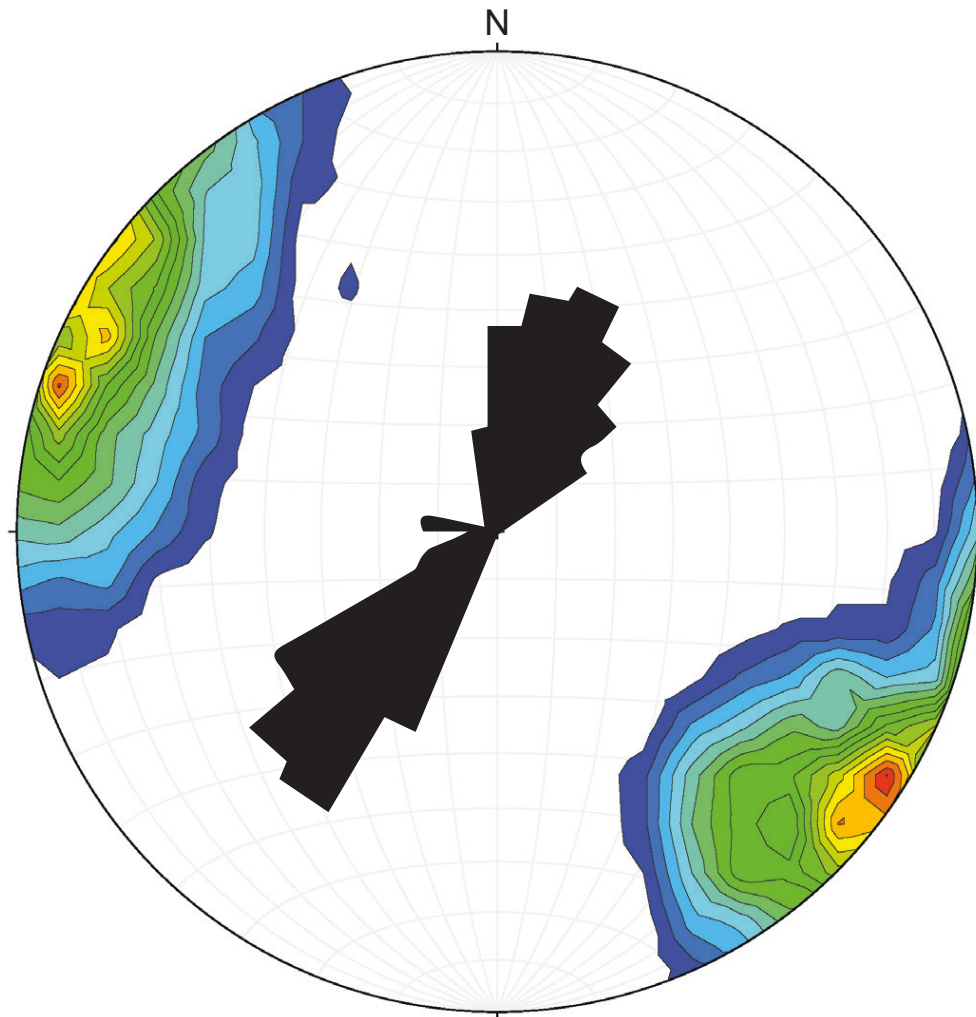
n=2094   Contour Interval: 2 sigma

Fig. 3. Orientations of mineralized fissures on an equal area stereonet with 2-sigma Kamb contours from the poles. Orientations are single measurements of mapped fissures, which are captured on every 15 m mine bench.

Many of the southern fissures have evidence of movement and are classified as faults. They can be continuous anywhere from 30 m to more than 2 km long and as deep as 900 m down from the pre-mine surface based on current data; however, they almost certainly continue beyond the open pit extent. Near the surface, they tend to be wider in all rock types (Field and Moore, 1971), which is a feature in late-stage sericitic veins of the Ann-Mason deposit (Nevada) as well (Dilles and Einaudi, 1992). Pre-mine topography shows that many of the large mineralized fissures formed topographic lows and valleys presumably due to the rapid weathering of sulfides.

In the southwest side of the deposit, fissure faults cut and displace all sedimentary units and the monzonite. In the northeast side of the deposit, fissure faults cut and displace the sedimentary units, latite porphyry dikes, and young quartz latite porphyry dikes. There are several older fault groups with their own distinctive orientations in the south side of the deposit, but none of them cut the fissures. One exception may be some East faults with a more prominent N-S strike, which are also late-stage. The southern fissures terminate against the large, lower angle, normal, Giant Chief fault that trends NW-SE, suggesting the Giant Chief fault likely prevented the fissure-related stress from being transmitted. Faults, like the Giant Chief, may have sulfide mineralization at intersections with fissures forming "pockets" of ore along the strike of the fault, though it is not extensive.

The dominant alteration type in the study area is propylitic, which is most obvious in the monzonite by secondary actinolite, chlorite, epidote, and calcite. The alteration is pervasive, but is most evident along joint surfaces as dark green coatings. The actinolite replaces both hydrous and anhydrous mafic minerals (Porter et al., 2012). The fissures cut this propylitic zone with localized sericitic and argillic alteration, as noted by Bowman et al. (1987). Mineralization is

generally poor in the propylitic zone, but near the fissures, the ore grades can be high enough to mine economically.

SAMPLING AND ANALYTICAL METHODS

In order to characterize the fissures and understand the origin, timing, and controls of their mineralization, six fissures were selected for in-depth study in the southwest wall of the Bingham pit (Fig. 2; Table 1). The general locations were largely determined by accessibility and safety. Care was taken to select representative fissures in each of the major host rocks. These were supplemented with data from other fissures collected by mine geologists in order to ensure proper characterization. In addition to sampling the fill material of each fissure, wall rock samples were taken on either side at 0.3, 1.5, 3.0, and 6.0 m distances. The target weight for each sample was 8-10 kg, which comprised several representative blocks of rock. Wall rock sampling on both sides of each fissure was done as a quality control in order to account for potential anomalies that would skew geochemical data. Important field observations were documented at each location including the characteristics of the fill material, thickness, nearby structures, pre- and post-fissure alteration, spatial fissure density, orientations, sense of shear, crosscutting relationships, and other influencing factors.

Five polished thin sections from each fissure were made (one from each of the sample intervals mentioned previously). The rocks chosen to make the thin sections were meant to be representative with preference given to samples that contained sulfide veinlets related to fissure mineralization.

From each 8-10 kg sample, 1 kg of representative material was selected and manually crushed to <10 mm while taking care to capture all fine material. All equipment was thoroughly cleaned in between each crushing and each of the subsequent steps. The samples were split using

Table 1. Details of fissures selected for study.

Fissure	Host Rock	Rock Unit	Width (cm)	Dip/Strike	Elevation (m)	Fault Product(s)	Avg Distance Between Fissures (m)[1]	Mineral Assemblage[2]
FF1	QZ	ILSU Quartzite	15	86°/38°	1917	breccia, powdered qz & sulfides	8.2	py>qz>ser>(ccp)
FF5	MZ	Phoenix Dike	15	86°/358°	1902	clay	7.3	py>qz>cal>ser>ccp>tnt
FF7	MZ	Phoenix Dike	150	74°/239°	1902	clay & powdered sulfides	8.6	py>qz>(ccp)
FF2	MZ	Phoenix Dike/ Last Chance Stock	10	78°/194°	2115	clay	8.3	py>ser>ccp>tnt>qz>gn>(ap)
FF3	LS	A-Bed	20	81°/199°	2115	breccia	8.1	py>gn>sp>cal>ccp>qz>tnt>ser
FF4	QZ	Highland Quartzite	10	83°/236°	2070	breccia, powdered qz & sulfides	4.3	py>qz>ab>ser>(ccp)>(gn)>(sp)>(ap)

Note: All sedimentary units are part of the Butterfield Peaks Formation

Abbreviations: QZ=quartzite, MZ=monzonite, LS=limestone, ILSU=intermediate upper limestone

[1] Determined by counting number of fissures per 200 m near sample area

[2] Minerals in parantheses were only found as inclusions in other minerals.

a riffle splitter, from which 100 g of material was powdered in a tungsten-carbide ring and puck pulverizer. The powders were dried overnight in a 105°C oven.

Whole rock analysis was completed by ALS Global in Vancouver. Gold concentration was determined by fire assay and atomic absorption spectroscopy (AAS). Heavily mineralized samples from the fissure fill material were dissolved by four-acid digestion and analyzed with an inductively coupled plasma atomic emission spectrometer (ICP-AES). This same analytical method was applied for select base metals (Ag, As, Cd, Co, Cu, Li, Mo, Ni, Pb, Sc, Tl, Zn) in wall rock samples. Other elements in the wall rocks were determined by lithium metaborate fusion followed by acid digestion and analysis by a combination of ICP-AES (for major elements) and ICP-MS (for trace elements).

Electron microprobe analysis (EMPA) of pyrite, chalcopyrite, tennantite, galena, and sphalerite were performed on a Cameca SX50 electron microprobe at Brigham Young University. The analytical conditions for the elements in each mineral varied and are summarized in Table 2. A 2-condition analysis was used on each spot in order to have lower detection limits for major and minor elements. The following natural standards were used: FeS_2 (Fe, S), CuFeS2 (Cu, Fe, S), GaAs (As), ZnS (Zn), PbS (Pb), and native Ag (Ag). $CuFeS_2$ was only used for the calibration of Fe and S in chalcopyrite with FeS_2 being used for Fe and S in all other minerals. These same grains were chosen for additional analysis by LA-ICP-MS and inspected by a combination of optical microscopy, scanning electron microscopy (SEM), and EMPA to ensure the grains were free of inclusions and cracks. Thin sections were used as opposed to grain mounts in order to preserve textural relationships. Sulfides in polished thin sections were analyzed on a Teledyne Analyte Excite 193 nm excimer laser ablation system coupled to an

Table 2. EMPA analytical conditions of fissure sulfides.

Mineral	Condition 1[1]				Condition 2[2]			
	Elements	kV	nA	Count Time (s)	Elements	kV	nA	Count Time (s)
Pyrite	S, Fe	20	10	20	Cu, As	20	100	60
Chalcopyrite	S, Fe, Cu	20	20	20	Zn, As	20	40	60
Tennantite	S, Cu, As	20	20	20	Zn, Fe	20	40	60
Galena	S, Pb	20	10	20	Cu, Ag, Zn	20	40	60
Sphalerite	S, Zn, Fe	20	20	20	Cu, As	20	40	60

[1] Used for major elements

[2] Used for minor to trace elements

Agilent quadrupole ICP-MS (7500 ce series) at the University of Utah. The ICP-MS was tuned while rastering across NIST610 glass prior to each session.

Laser ablation conditions varied depending on the minerals being analyzed. Each spot was pre-ablated with two shots to remove contaminants and the spot size was 40-50 µm. The frequency varied between 5-7 Hz, while fluency ranged 5-7 J cm^{-2}. Significantly lower fluency has been used by other workers particularly for softer sulfides (Maydagán et al., 2013; George et al., 2015; George et al., 2016; George et al., 2018). However, adequate ablation and signal peaks could not be attained until using a higher fluency similar to Cook et al. (2009b). The total analysis time was 90 s for pyrite (20 s background, 70 s ablation) with a 30 s washout time in between shots. For chalcopyrite, sphalerite, tennantite, and galena the analysis time was 70 seconds (30 s background, 40 s ablation) with a 30 s washout time in between analyses.

On occasion, the laser ablated through the grains towards the end of the ablation time showing these conditions were not always ideal for thin section work. Consequently, a lower fluency or using thicker sections is recommended for future analyses of sulfides where preservation of textures is important. A strong and abrupt Na peak was consistently present immediately after ablating through a grain. This was therefore monitored closely during each spot analysis and flagged to ensure the data that followed the Na peak were not included during data reduction.

Each pyrite grain was analyzed at both the core and the rim. For chalcopyrite, sphalerite, tennantite, and galena, 1-2 spots per grain were analyzed, but not always in consistent locations due to the amount of inclusions, fractures, and overall smaller grain size of these minerals. Following the precautions of Cook et al. (2016), tennantite and galena were analyzed last to avoid high background counts of As and Pb in subsequent analyses. The following isotope suite

was analyzed, based largely on those selected by Cook et al. (2009a) and George et al. (2016) for sulfides: ^{34}S, ^{51}V, ^{52}Cr, ^{55}Mn, ^{57}Fe, ^{59}Co, ^{60}Ni, ^{65}Cu, ^{66}Zn, ^{69}Ga, ^{75}As, ^{78}Se, ^{95}Mo, ^{107}Ag, ^{111}Cd, ^{115}In, ^{118}Sn, ^{121}Sb, ^{125}Te, ^{182}W, ^{193}Ir, ^{197}Au, ^{202}Hg, ^{205}Tl, ^{208}Pb, and ^{209}Bi. The dwell times varied with 0.05 s for Au, 0.005-0.02 s for major elements, and 0.02 s for all other elements.

MASS-1 served as an external standard and was analyzed three times before and after each set of 10 analyses, or when moving to a different mineral. The use of MASS-1 as a standard for LA-ICP-MS analysis of a variety of sulfides has been widely applied (Maydagán et al., 2013; Franchini et al., 2015; George et al., 2016; Rottier et al., 2016; George et al., 2018; Wu et al., 2018). The concentrations of elements from the most recent USGS certificate of analysis were used for all elements except Au. Gold has been removed from the certificate of analysis after discovering it was heterogeneously distributed in MASS-1 (S. Wilson, pers. commun., 2018). This heterogeneity was most obvious when performing ablation lines, but otherwise appeared consistent during spot analysis. As such, the original concentration of Au from Wilson et al. (2002) was used for MASS-1 during data reduction. Reported values of Au in this study should therefore be taken with caution.

Data was reduced using Iolite v2.5 (Paton et al., 2011) for Igor Pro with internal standard values determined by separate microprobe analysis. The internal standards were as follows: Fe (pyrite), Cu (chalcopyrite, tennantite), Pb (galena), and Zn (sphalerite). Data from each analysis was investigated for sharp, anomalous peaks that were inconsistent throughout the ablation time of each shot. These were flagged as potential inclusions and ignored during data reduction. Data were further validated by treating every third MASS-1 analysis as an unknown and monitoring the relative standard deviation and the percent error from the certified values for the MASS-1 analyses treated as calibration standards.

Sulfur and oxygen isotope analyses were performed on pyrite and quartz separates from each of the fissures. These minerals were selected as they were abundant and ubiquitous in each fissure regardless of location. Calcite was commonly present as well; however, Bowman et al. (1987) suggest the that the calcite at Bingham (in veins or rock matrix) is too enriched in ^{18}O to reasonably be in isotopic equilibrium with silicate and sulfide minerals. As such, it was not included in our isotopic analyses.

To acquire mineral separates, samples of the fissure fill material were selected that were free of wall rock. The samples were crushed to 16-mesh and separated using a combination of gravimetric and heavy liquid techniques to acquire 0.5 g of each mineral. The quartz separates were additionally washed in dilute HCl to remove any calcite coatings. Each mineral grain was visually inspected under microscope to ensure it was free of other minerals or obvious inclusions. The mineral separates were analyzed by the Queens Institute for Isotope Research in Kingston, Canada. Quartz separates were heated under vacuum to decrepitate any fluid inclusions, and were then pulverized to a fine powder. Pyrite separates were assumed to have no fluid inclusions that could skew S isotope compositions. The sulfur isotopic composition was measured using a MAT 253 Stable Isotope Ratio Mass Spectrometer coupled to a Costech ECS 4010 Elemental Analyzer with $\delta^{34}S$ reported relative to the Vienna Canyon Diablo Troilite (VCDT). Oxygen was extracted following methods of Clayton and Mayeda (1963) and analyzed on a Thermo-Finnigan Delta^{Plus} XP Isotope Ratio Mass Spectrometer with values reported relative to the Vienna Standard Mean Ocean Water (VSMOW).

PHYSICAL CHARACTERISTICS OF FISSURES

Characteristics of the fissures were studied on both a macro- and microscopic scale, which ranged anywhere from the mine extents down to those only observable by SEM imaging. There are similarities between all of the fissures, which is why they were initially grouped

together over a century ago (Boutwell, 1905). Nonetheless, variations exist over a wide range of scale in terms of structures, textures, and mineral assemblages. These are most closely related to the host rock and proximity to the center of the deposit.

Macroscopic physical characteristics

      The fissures are 1 cm to greater than 1.5 m wide veins filled with sulfides and gangue minerals (Fig. 4). The vein width along individual fissures can vary considerably even from one mine bench to another. Smaller sulfide veinlets are common in the adjacent wall rock and run both parallel and perpendicular to the main fissure veins (Fig. 4a). Sulfide mineral abundance along these veinlets, and in general, decreases sharply with increasing distance from the mineralized fissure veins. Several prominent, unmineralized joint sets are found in conjunction with these fissures with one set always roughly parallel to the fissure orientation. Faulting along the fissures was normal based on the offset of sills, and slightly oblique as evidenced by subparallel slicken-lines; however, the offset is typically minimal compared to older major faults in the deposit. Faulting is often associated with lithological contacts based on extensive mapping by mine geologists and observable fault products (breccia, gouge, etc.). This is especially evident where dikes of monzonite are juxtaposed against sedimentary rocks. The majority of these dikes show the same general alignment with the fissures and can be bounded by faults on either side.

      Differences are observed where the fissures run through different rock types. Simple line scans yield an average spacing of 7.5 m between fissures in all rock types, but in the quartzites this spacing is as small as 4.3 m (Table 1). Quartzite appears to be more brittle than the monzonite or limestone. This causes fissures to splay more with more intense brecciation (Fig. 4a). The result is a higher spatial density and fissure "swarms" (Fig. 4d). Additional fault products include pulverized wall rock and sulfides, which can range anywhere from sand- to clay-sized particles (Table 1).
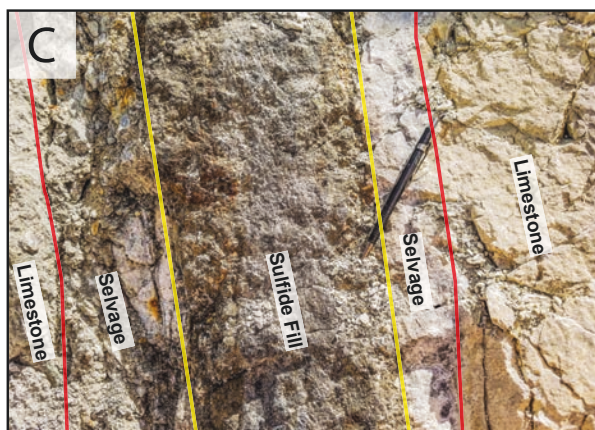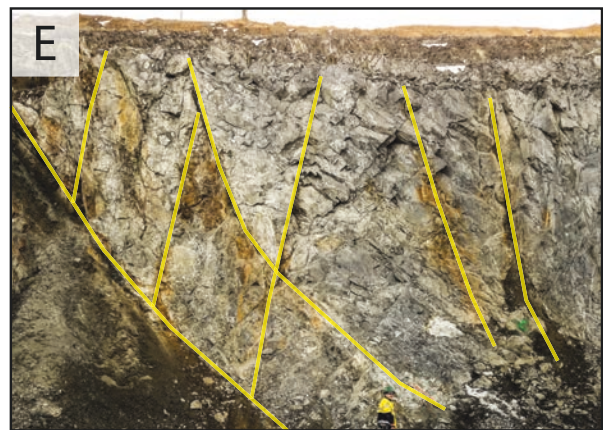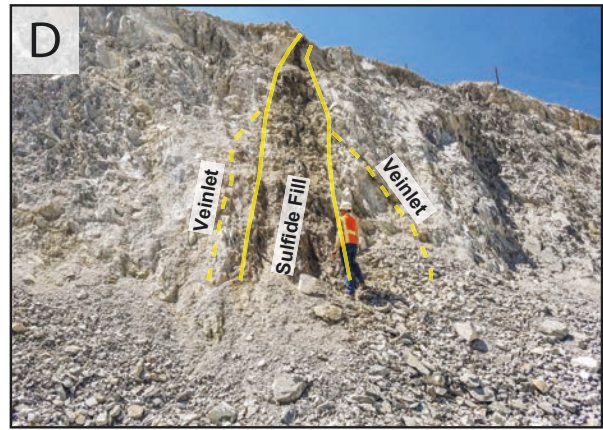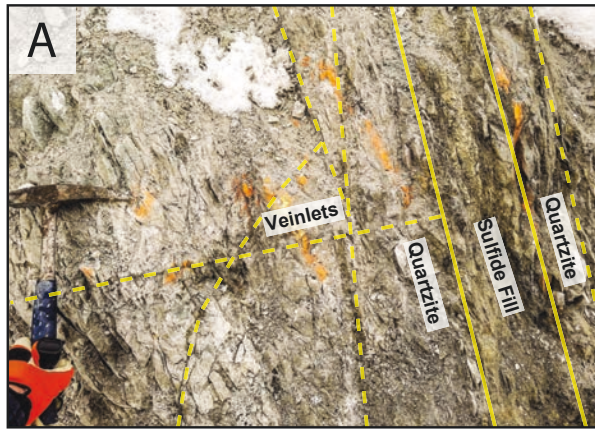
Fig. 4. Macroscale features of fissure mineralization at the Bingham deposit. A. Intense brecciation and fracturing in a quartzite-hosted fissure with small pyrite and quartz veinlets that are both perpendicular and parallel to the fissure. B. Wide quartz and sericite selvages bounding a monzonite-hosted fissure that are weak, friable, and lighter in color relative to the darker unaltered wall rock. C. Zoned limestone-hosted fissure with galena, pyrite, chalcopyrite, and sphalerite in the middle with predominately pyrite towards the edges followed by a light colored silicified selvage. D. A large fissure that splays into a few smaller sulfide veinlets. E. Example of a fissure "swarm" in propylitically altered monzonite. Such swarms are observed in all rock types, but particularly in quartzite. F. A fine-grained sulfide block separated from a fissure with interstitial quartz shows how large and competent these mineralized bodies can be.

The visible alteration of the wall rock results in a lighter colored selvage due to an abundance of quartz, sericite, and sometimes calcite in the adjacent monzonite (Fig. 4b) and limestone (Fig. 4c). Quartzite appears largely unchanged at the outcrop scale (Fig. 4a) except when the fissures pass through oxidized quartzite units, which also results in a lighter colored selvage. The fill material in the quartzite is dominated by pyrite and quartz, which are found in all the fissures. The fissures in monzonite additionally have chalcopyrite, clay, and sericite, while the limestone-hosted fissures have pyrite, chalcopyrite, galena, sphalerite, and calcite (Fig. 5). Other mineralogical variations exist at the microscopic scale and are discussed in the following section.

Microscopic physical characteristics

There are many observations at the microscopic scale that are common amongst all fissures regardless of host rock or distance from the center of the deposit. The dominant sulfide is euhedral pyrite with a single preferred interstitial gangue mineral that varies between sample locations. The sulfides are fine-grained not normally exceeding 1.5 mm across, while averaging 0.5 mm. Sulfides were strongly fractured and then healed by gangue minerals, and less-commonly other sulfides such as chalcopyrite and tennantite (a copper arsenic sulfosalt mineral). The microfractures parallel the fissures, creating microbreccia "channels" through the fissure fill material (Fig. 6a). Mineral inclusions are seen in all of the sulfides, which frequently form "trails" that mimic mineral growth patterns on the outer edges of their hosts (Fig. 6b). Vugs (possibly fluid inclusions) are also present in pyrite grains, though their placement in the grains is more random. What is also common amongst all fissure samples are chalcopyrite and quartz inclusions (~10-20 μm) hosted within pyrite grains (Fig. 6c). Mineralization in the host rocks is restricted to small veinlets that decrease in size, sulfide abundance, and quantity with increasing
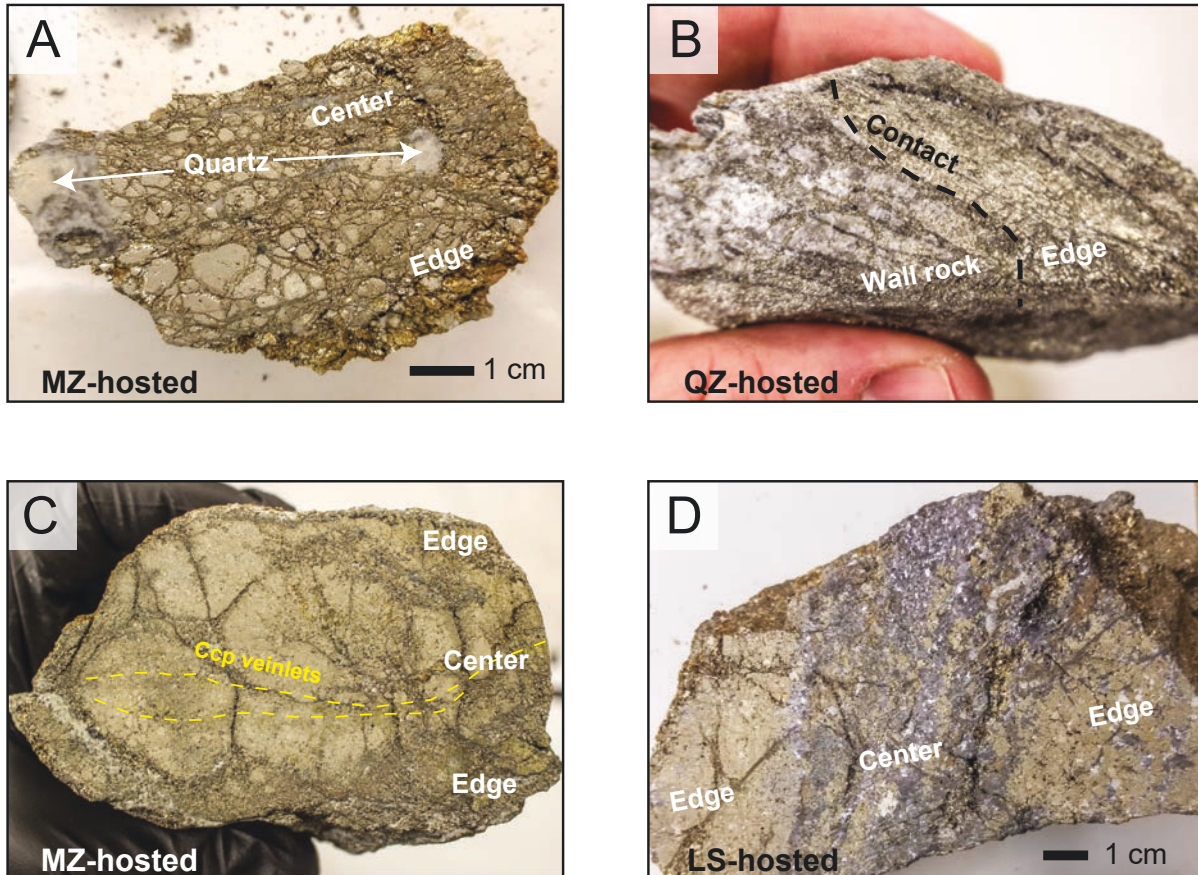
Fig. 5. Slabs cut from the fill material of various fissures. A. Monzonite-hosted fissure from the porphyry environment with quartz-filled vugs and fractures. B. The contact between the edge of a fissure and quartzite wall rock in the porphyry environment. Small sulfide veinlets go into the wall rock. C. Fissure from the epithermal environment with sericite on the edges where it meets monzonite wall rock and small chalcopyrite veinlets that parallel the fissure orientation. D. Limestone-hosted fissure from the epithermal environment with pyrite-dominated edges and abundant galena and sphalerite towards the center.
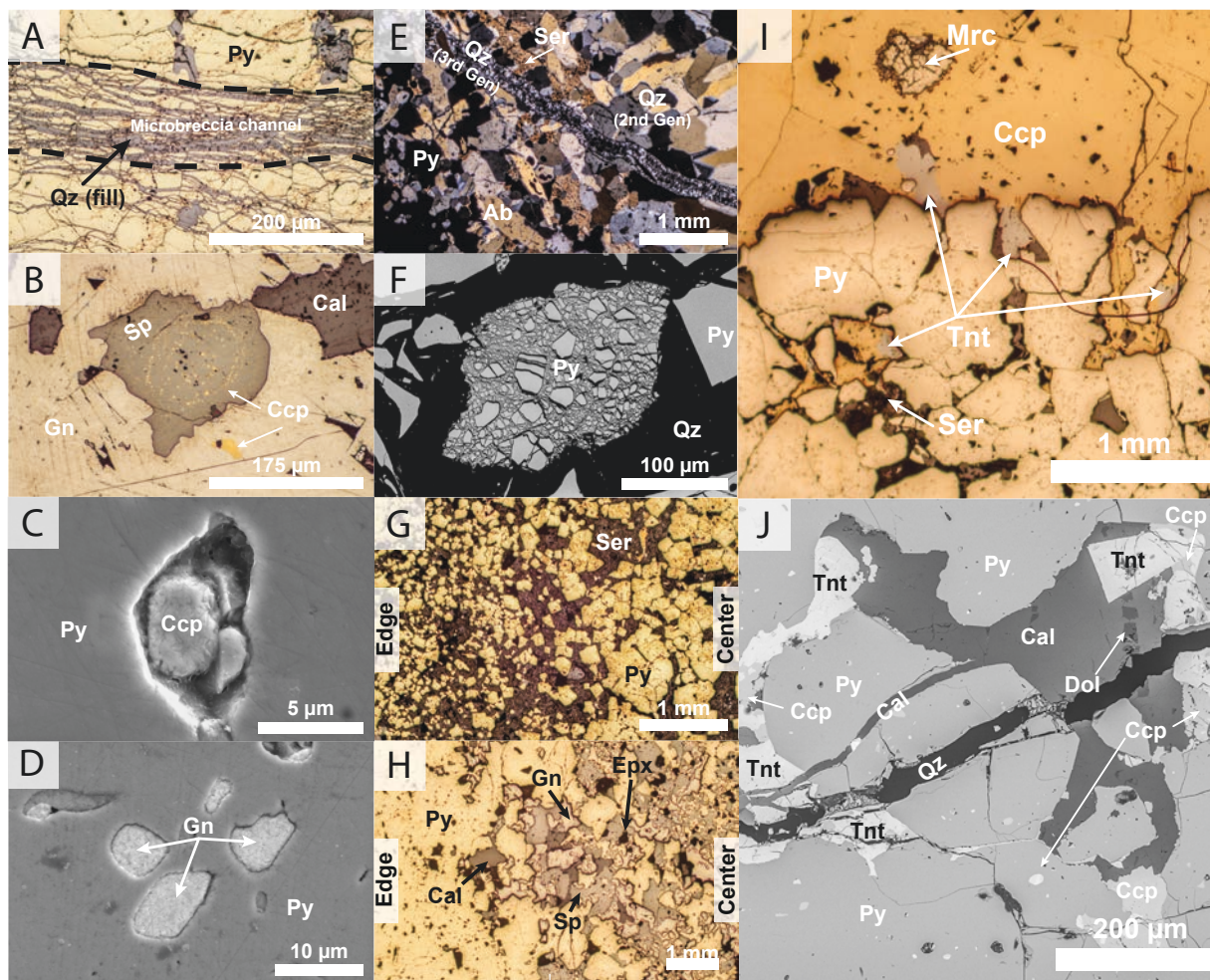
Fig. 6. Microscale features of the sulfide fill of fissures at the Bingham deposit. A. Microbreccia "channels" are found in all rock types and run parallel to the associated fissures (reflected light). B. Sphalerite grain from the epithermal environment with chalcopyrite inclusions that form rings that mimic crystal faces (reflected light). C. Typical chalcopyrite inclusion in a pyrite grain (SEM image). D. Galena inclusions in a pyrite grain that only appear outside the Pb-Zn boundary shown in Fig. 2 (SEM image). E. Quartz veinlet cutting across an earlier generation of quartz, sericite, albite, and pyrite (cross-polarized transmitted light) F. Complete shattering of a single pyrite grain from a fissure with evident faulting (SEM image). G. Fining outward trend of pyrite grains in a monzonite-hosted fissure with increasing amounts of interstitial sericite as the altered wall rock is approached (reflected light). H. Fining inwards of sulfides in a limestone-hosted fissure, which is also associated with zonation of pyrite on the edges and galena, sphalerite, calcite and pyrite in the center (Fig. 4c) (reflected light). I. A chalcopyrite veinlet next to pyrite in a monzonite-hosted fissure with textures of chalcopyrite and tennantite indicating they are late-stage (reflected light). J. Another example of the association and textures of chalcopyrite and tennantite, which are found close to a small third-generation quartz veinlet (BSE image). Py-pyrite, Sp-sphalerite, Cal-calcite, Gn-galena, Ccp-chalcopyrite, Ser-sericite, Ab-albite, Epx-epoxy, Mrc-marcasite, Tnt-tennantite, Dol-dolomite.

distance from the main fissure. Most sulfides disappear completely from these veinlets within 3 m of the fissure vein, at which point non-sulfide gangue minerals dominate.

Three distinguishable generations of quartz are present, which is determined by cross cutting relationships, grain size, and scanning electron microscope cathodoluminescence (SEM-CL) imaging (Fig. 7). The first generation is found near the fissure-wall rock selvage. It has euhedral grains, but SEM-CL imaging reveals resorbed and embayed, bright cores with dull, euhedral rims. The second generation of quartz is made of euhedral grains with oscillatory zoning forming clusters mixed with pyrite. The third generation is very fine-grained and restricted to small interstitial veinlets that have healed the fracture networks (Fig. 6e). Networks of smaller, secondary quartz veinlets are also found in the main ore body and are associated with late Cu-Fe sulfide precipitation (Landtwing et al., 2005).

Chalcopyrite and tennantite grains that are not found as mineral inclusions are always anhedral and found in conjunction with one another (Fig. 6i). Their textures indicate they were late-stage relative to the other sulfides and that tennantite is often a replacement product of chalcopyrite (Figs. 6i and 6j). They are concentrated along healed fractures and also fill interstitial space. The replacement of chalcopyrite by tennantite also occurs in the late stage alteration related to skarns in the Commercial and Jordan limestones on the west side of the deposit (Atkinson and Einaudi, 1978). This replacement is consistent with textures and mineral assemblages associated with an intermediate-sulfidation environment found in transition zones from porphyry to epithermal environments (Muntean and Einaudi, 2001; Einaudi et al., 2003; Sillitoe, 2010; Maydagán et al., 2013).

Microscopic differences between the fissures are related to distance from the center of the deposit and the host rock. This is primarily manifested by variation in mineralogy in the fissure
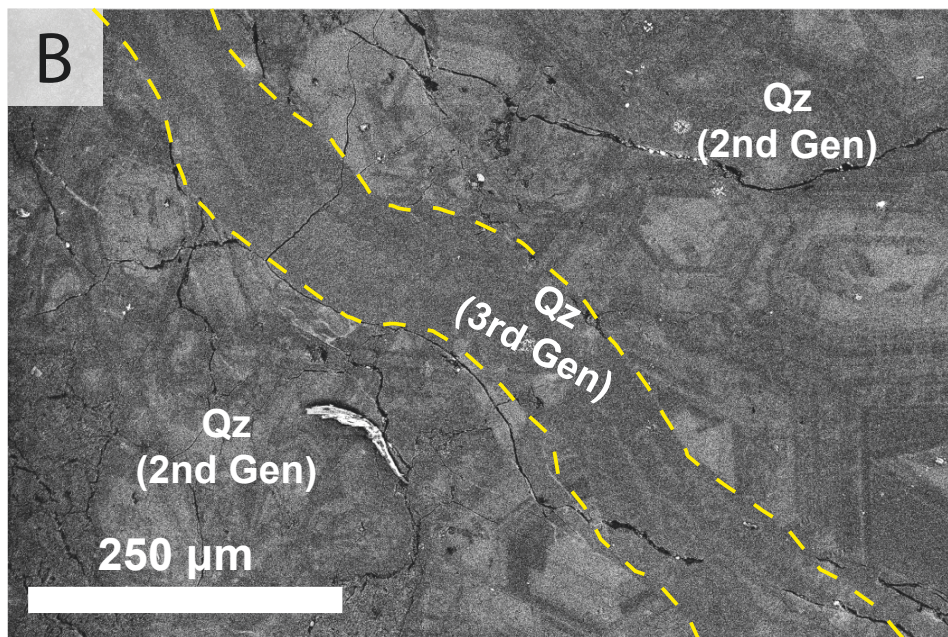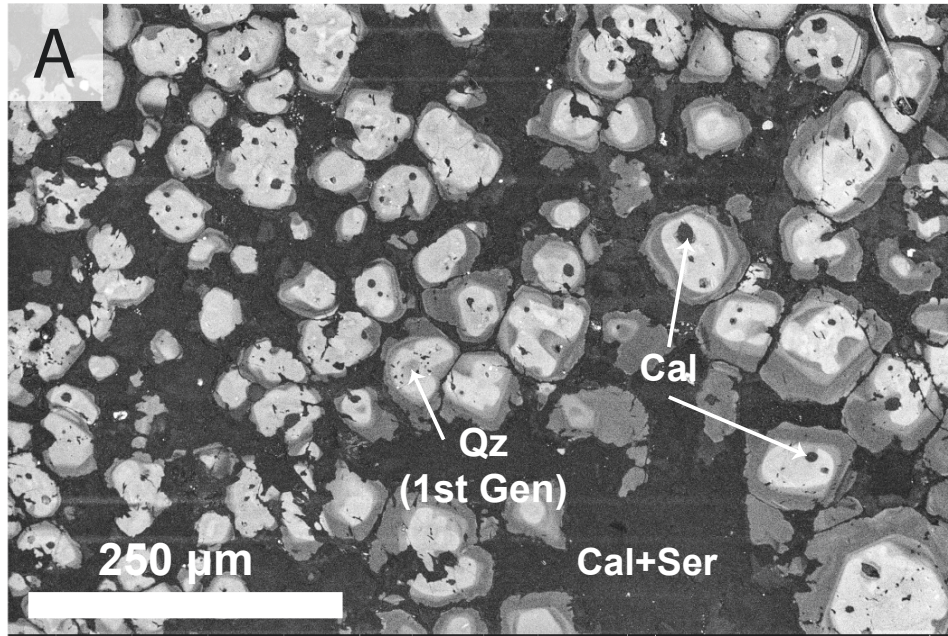
Fig. 7. SEM-CL images of three generations of quartz grains in the Bingham fissures. A. The first generation of quartz is identified based on CL brightness and textures, and is found near the wall rock selvage. Rounded and embayed cores (bright) indicate precipitation from hotter hydrothermal fluids followed by dissolution near the selvages. These were overgrown by lower temperature quartz (dark) with more euhedral faces. B. The second and third generations of quartz are identified based on cross cutting relationships and CL brightness (see Fig. 6e). The second generation is also bright with oscillatory zoning and large euhedral grains, while the third generation has a dull luminescence and is finer grained.

23

fill, fissure-associated veinlets, sulfide-hosted inclusions, and alteration products. Other variations include the intensity of brecciation, sulfide grain size, and zonation of the fissure fill as discussed below.

The appearance of galena and sphalerite—as inclusions or separate grains—is restricted to the fissures farthest from the center of the deposit (FF2, FF3, and FF4; Figs. 5d and 6d). A crude Pb-Zn boundary was drawn to illustrate where this occurs and was further extrapolated based off Pb and Zn assays. This likely represents the transition from a porphyry to an epithermal environment characterized by lower temperature fluids and increased Pb-Zn-Ag mineralization (Figs. 1 and 2). Fissure zonation related to Pb and Zn also occurs in the Tintic mining district (Hildreth and Hannah, 1996); however, this is by no means a unique observation. Metal zonation of porphyry deposits can have several complicating factors, but it appears to be largely temperature-controlled with the following pattern from proximal to most distal of the center of the deposits: Cu-Mo, Cu, Pb-Zn, Au-As/Au-Ag (Atkinson and Einaudi, 1978; Audétat et al., 2000; Seedorf, 2005; Sillitoe, 2010; Mao et al., 2011; Catchpole et al., 2015).

Tennantite generally appears in the fissures at this same boundary, though minor tennantite was found in a monzonite-hosted fissure (FF5) slightly closer to the center of the deposit. The amounts of galena and sphalerite increase with increasing distance from the center of the deposit. These were the primary ore minerals for the early underground workings on the southern outer edges of the current pit. Such heavy mineralization of Pb-Zn further indicates an intermediate-sulfidation environment (Einaudi et al., 2003). North of this boundary, galena and sphalerite are not found in the fissures as inclusions or as separate grains. South of the Pb-Zn boundary fissures also had the most chalcopyrite overall, despite it being present in all samples.

One of these (FF2) had a continuous chalcopyrite veinlet in the center of the fill material that paralleled fissure orientation (Fig. 5c).

Quartzite-hosted fissures contain the simplest mineral assemblages with pyrite and quartz dominating and minor sericite, albite, and chalcopyrite. Mineral inclusions in the pyrite include quartz, chalcopyrite, apatite, albite, and anhydrite. Brecciation is most intense in the quartzites even at the micro scale, which produces micro faults and complete shattering of individual grains that are not as readily observed in other rock hosts (Fig. 6f). The effects of hydrothermal alteration on the quartzite is minimal manifested primarily by secondary quartz, sericite, calcite, and sulfides in veinlets and some interstitial space. The veinlets show a transition in mineral proportions with distance from the fissure. They begin with pyrite>quartz>sericite within 0-1.5 m, transitioning to quartz>sericite>pyrite within 1.5-3.0 m, and ending with sericite>quartz at 6 m.

Monzonite-hosted fissures have pyrite as the dominant sulfide with minor chalcopyrite and the most tennantite overall. The dominant interstitial gangue mineral in the fill material is not consistent and varies between sericite (FF2), calcite (FF5), and quartz (FF7). In addition to multiple generations of quartz, the calcite and sericite appear to have two generations (one filling interstitial space and the other healing fractures), which cut the 1st and 2nd generation of quartz and sulfides. These fissures have the largest mineral grains (sulfides and gangue minerals) relative to the other rock types. The largest grains are consistently in the center of the fill material and grade out to more fine-grained material on the edges (Fig. 6g). This reduction in grain size is accompanied by an increasing abundance of gangue minerals (typically sericite) as the wall rock is approached (Fig. 5c). Immediately following the sericite, the fissure selvage is dominated by quartz with sericite becoming more restricted to small veinlets between sulfide and quartz grains. The wall rock quickly transitions back to its regular appearance within 0.3-1.5 m,

but small pyrite-quartz-sericite veinlets can continue past 12 m depending on the size of the fissure. Biotite grains proximal to these veinlets are chloritized. These veinlets change in mineral proportions with distance similar to those hosted in the quartzites with the sulfides being the first to disappear and ending with sericite dominating. The abundance of sericite in the monzonites, whether in the veins or altered wall rock, is significantly higher than in any of the other rock types.

Limestone-hosted fissures also have pyrite as the dominant sulfide, though in smaller abundances as they can also have significant galena and sphalerite with minor chalcopyrite in the epithermal environment. The amount of pyrite relative to these other sulfides increases with depth in the limestone-hosted fissures (Field and Moore, 1971), and nearer the center of the deposit. The chalcopyrite is present as anhedral grains, but also as inclusions in sphalerite (Fig. 6b). This has been referred to as "chalcopyrite disease," which is believed to form as a result of co-precipitation of the two sulfides or replacement of sphalerite (Bortnikov et al., 1991). The abundance of these chalcopyrite inclusions illustrates how several inclusions align themselves with crystal growth planes. The dominant interstitial minerals are calcite and dolomite with lesser amounts of quartz and sericite. Unlike the other rock types, the limestone-hosted fissures can have large galena and sphalerite grains similar in size to the pyrite rather than being present only as inclusions or within small veinlets. These fissures are also zoned with large pyrite grains on the outer edges that fine inward towards the center of the fill material (Fig. 5d). The center is a fine-grained mixture of pyrite, galena, and sphalerite in roughly equal proportions and anhedral crystal shapes (Fig. 6h). This zonation suggests Pb-Zn mineralization occurred late and at lower temperatures. In this center mixture, each sulfide was found with inclusions of the others indicating co-precipitation. The contact between the fissures and the limestone wall rock is

generally quite sharp. The selvage is dominated by complete silicification of the limestone, which fades out within <1 m. This silicification is cut by small sericite-sulfide-carbonate veinlets. The sulfides disappear from the veinlets in the wall rock after about 3 m and transition to just sericite and carbonate minerals.

CHEMICAL CHARACTERISTICS OF FISSURE ORES

Major and trace element compositions were analyzed in whole-rock samples and individual sulfide grains from the fissure fill. As with the physical characteristics, many elemental trends of the fissure fill material are associated with distance from the center of the deposit and the host rock. The altered wall rocks adjacent to mineralized fissures show several trends as well, which are important for determining the extent of fissure-associated alteration and how these ore bodies can be defined.

Whole-rock geochemistry of fissure ores

The sulfide-rich fill material of each fissure contains the highest Ag, As, Au, Bi, Cd, Cu, Fe, Pb, Sb, and Zn relative to the associated wall rocks (Table 3). Tin was not analyzed in the fissure fill, but the wall rock concentrations of Sn all trend higher toward the fissure indicating it is likely high in Sn as well. This confirms the fissures are the source of the Cu-Ag-Au ore, and that ore is most likely hosted within sulfides and sulfosalts since they make up the majority of the fill material (typically >90%). Gold concentrations are positively correlated with Ag, As, and Cu (Fig. 8.), which suggests the Au may be hosted in a mineral phase rich in those elements such as tennantite—this was investigated in the sections that follow. Most of these elements (excluding Fe) also increase with increasing distance from the center of the deposit in the fissures and show loose positive correlations with each other. The strongest correlations are with Ag, As, Bi, Pb, and Zn, which are highest in limestone-hosted fissures along with Sb and Cd; the

27
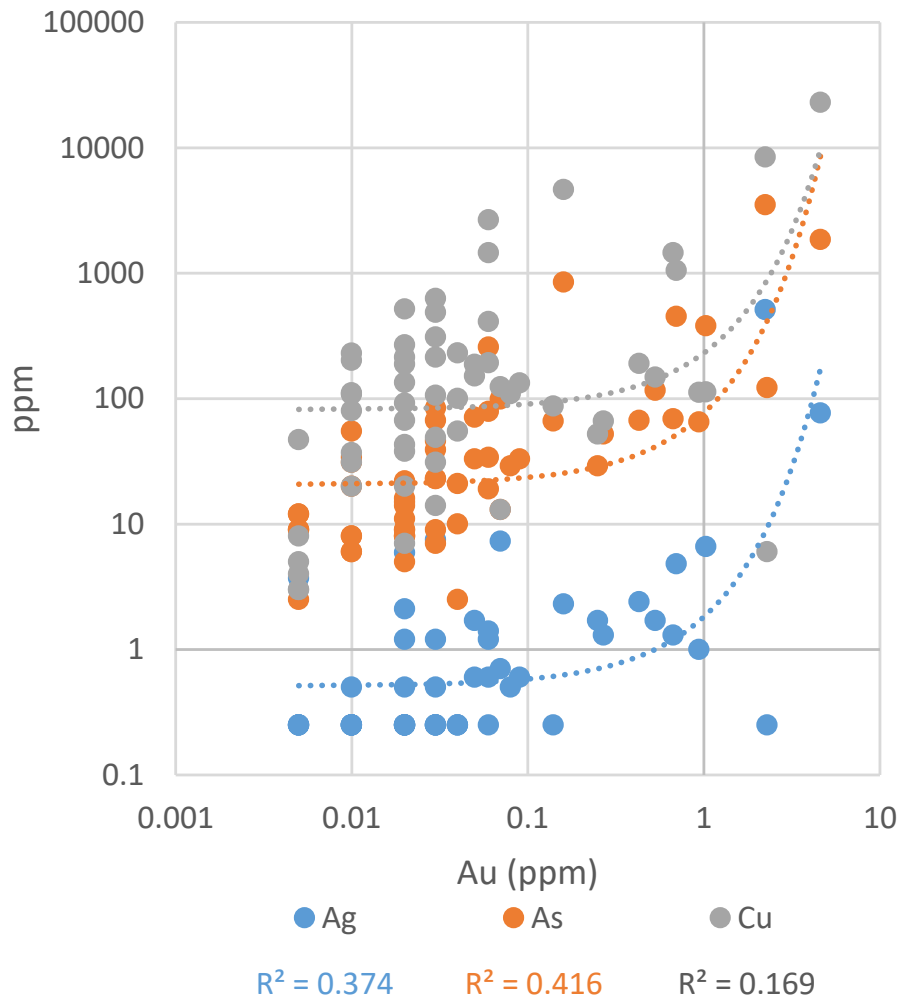
Fig. 8. Logarithmic plot of Ag, As and Cu vs Au from whole rock analyses of fissures and associated wall rocks up to 6 m from the edge of each fissure. All of these elements show positive correlations with Au, which is strongest with As.

Table 3. Select whole rock chemical analysis of fissure fill material

Host Rock		Porphyry[1]			Epithermal[1]		
		QZ	MZ	MZ	MZ	LS	QZ
Sample		FF1-C	FF5-C	FF7-C	FF2-C	FF3-C	FF4-C
Ag	ppm	1.30	1.30	1.00	76.8	511	6.60
As	ppm	52	69	65	1855	3510	380
Au	ppm	0.27	0.67	0.94	4.61	2.24	1.03
Ba	ppm	5.0	0.5	0.5	50.0	0.5	0.5
Bi	ppm	10	20	10	115	389	16
Cd	ppm	0.3	0.9	1	2.5	274	0.8
Co	ppm	21	43	23	44	8	19
Cr	ppm	0.5	1	0.5	42	0.5	3.0
Cu	ppm	66	1450	112	23000	8430	113
Ga	ppm	0.5	1	0.5	20.0	0.5	0.5
La	ppm	0.5	1	0.5	10	0.5	20.0
Mn	ppm	2.5	277	2.5	518	313.0	2.5
Mo	ppm	0.5	1	1	3	1	1
Ni	ppm	3	5	4	20	2	2
P	ppm	5.0	20	5	1310	10	10
Pb	ppm	135.0	51	190.0	853.0	>200000	681.0
Sb	ppm	2.5	7	12	30	513	14.0
Sc	ppm	1	1	1	5	1	1
Sr	ppm	0.5	8.0	0.5	12.0	1.0	2.0
Th	ppm	10	10	10.0	10.0	10.0	10
Tl	ppm	1	1	1	1	0.5	1
U	ppm	20	1	10	30	1	1
V	ppm	1	1	1	49	1	4
W	ppm	210.0	130	280.0	230	90	310.0
Zn	ppm	20	12	183	246	57400	317
Al_2O_3	wt%	0.13	0.11	0.08	4.65	0.04	0.74
Fe_2O_3	wt%	56.33	58.91	51.47	50.61	36.74	50.90
CaO	wt%	0.11	3.71	0.01	2.43	1.26	0.04
MgO	wt%	0.02	0.02	0.01	1.53	0.02	0.02
Na_2O	wt%	0.01	0.01	0.01	0.01	0.01	0.01
K_2O	wt%	0.04	0.04	0.02	1.13	0.01	0.20
TiO_2	wt%	0.01	0.01	0.01	0.22	0.01	0.01

Notes: Certainties vary between elements due to the variety of
analytical methods used; values below detection limits (typically 1
[1]Contact between porphyry and epithermal stage shown in Fig. 1 as

concentrations of these elements can be several orders of magnitude higher than in the other host rocks, which remains true even when comparing fissures from the epithermal environment. The monzonite-hosted fissures contain the most Co, Cr, Cu, Fe, Ni, P, Sr, and U, while the quartzite-hosted fissures contain the most W (Table 3).

The sharpest increase in all of these enriched elements (Ag, As, Au, Bi, Cd, Cu, Pb, Sb, and Zn) occurs at the Pb-Zn boundary (Fig. 2), which is accompanied by a shift in metal ratios (Table 4). The average Ag:Au ratio of fissure ore sampled inside the Pb-Zn boundary (Fig. 2) is 16:1, while the average of those beyond the boundary is 79:1. This high Ag:Au ratio is further evidence of a transition to an intermediate-sulfidation epithermal environment, which have Ag:Au ratios typically around 100:1 (Einaudi et al., 2003). The Cu:Au ratios also show a strong contrast between the two environments. The porphyry environment has an average Cu:Au ratio of 10,300:1 while the epithermal environment has an average ratio of only 2,333:1.

Whole rock geochemistry of wall rocks

The fissures have a strong, but not laterally extensive visual effect on wall rocks (Fig. 4), which was also observed by Field and Moore (1971). This is further confirmed by geochemical data, which was collected at set intervals away from the fissures at each location. Fissure-related alteration and mineralization can extend into the wall rock from as little as 0.3 m to greater than 12 m, although on average the effects do not extend past ~1.5 m. This range is also considering small veinlets related to the fissures mentioned previously.

Isocon diagrams (Grant, 1986) illustrate these geochemical changes (Fig. 9). Samples closest to the fissure are obviously enriched in ore metals (Ag, Au, and Cu) as well as As, Cd, Cr, Fe, Pb, Sn, W, and Zn. They are also depleted in soluble alkalis (Na, K, Rb, and Cs) and alkaline earths (Ba, Sr). By 3.0 m away from the fissure, the wall rocks essentially return to their original compositions, which aligns with visual observations. The only exception was for an
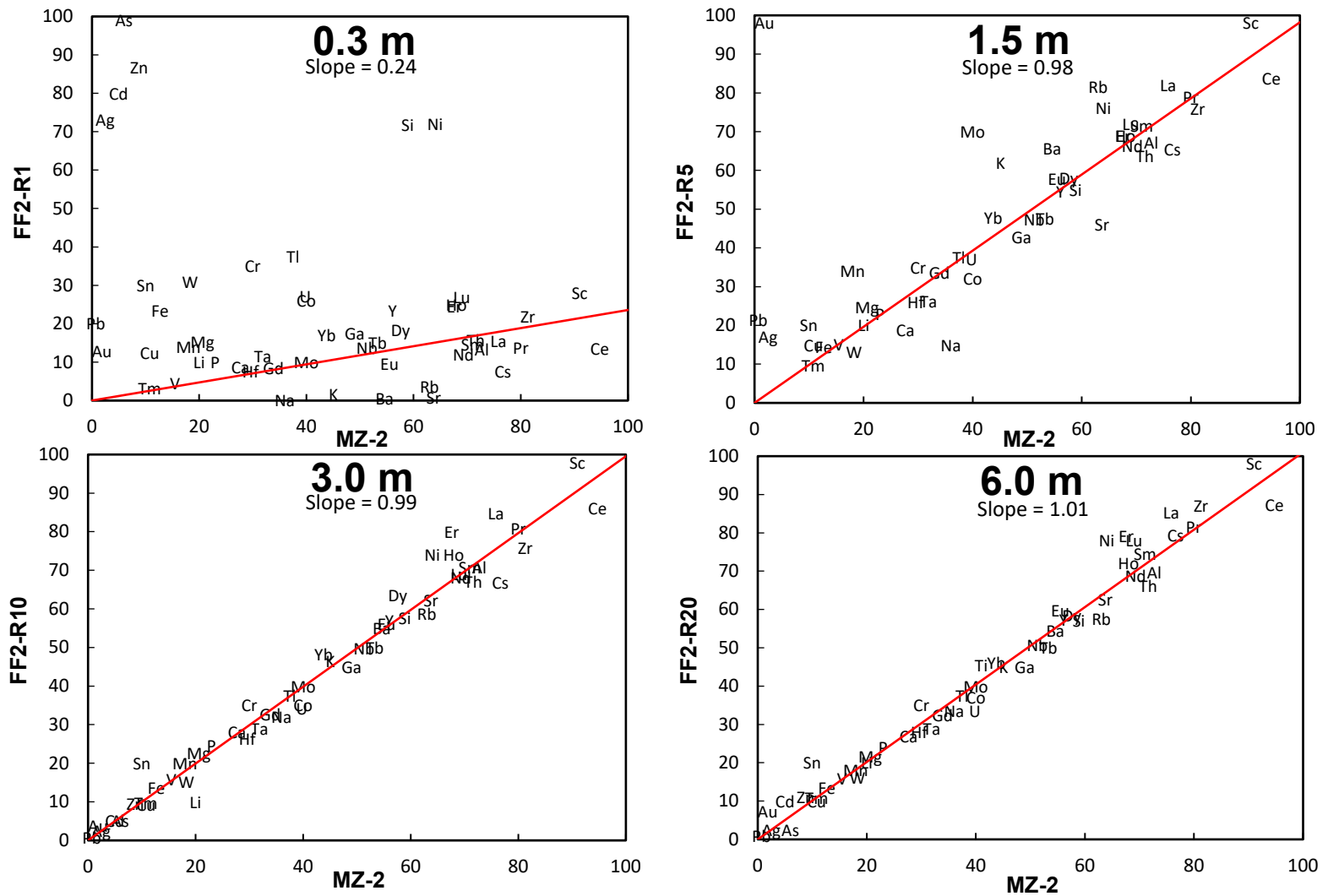
Fig. 9. Isocon diagrams for monzonite wall rock at intervals away from a mineralized fissure (FF2). A propylitically altered monzonite sample that was known to be geochemically unaffected by fissures was chosen to represent the original composition (MZ-2). The red line represents the isocon, which is drawn along HFS elements that show immobile behavior during hydrothermal alteration (Zr, Hf, Nb, and REE). Elements above the isocon indicate enrichment, while those below indicate depletion. Element concentrations are arbitrarily scaled. The high silica content of the sample at 0.3 m (72 wt% vs 56 wt%) diluted the immobile elements causing a shallower slope for the isocon. Silicification is not obvious at 1.5-6.0 m; Si lies near the isocon and the slopes of the isocons are nearly 1:1.The effects of the fissure on the monzonite wall rock are noticeable up to 1.5 m (e.g., enrichments of Au, Ag, Mo and depletion of Na), but are largely unrecognizable by 3.0 m.

Table 4. Whole rock metal ratios of fissure ore.

Host Rock Fissure	Porphyry[1]				Epithermal[1]			
	QZ FF1	MZ FF5	MZ FF7	Average	MZ FF2	LS FF3	QZ FF4	Average
Ag:Au	29	11	10	16	25	199	14	79
Cu:Au	10600	9200	11100	10300	2900	2500	1600	2333

Notes: Metal ratios are calculated from the fissure vein and surrounding wall rock samples

[1]Contact between porphyry and epithermal stage shown in Fig. 1 as Pb-Zn boundary

abnormally large fissure (FF7, Fig. 4d) with a width of ~1.5 m, which had heavy sulfide

mineralization along joints up to 12 m away. While this may indicate a correlation between

fissure width and ore body size, it is not as common for the fissures to reach such thicknesses.

The restricted lateral effects on the wall rock are true for fissures regardless of rock type or

proximity to the center of the deposit. Despite this, the distance from the center of the deposit and

the host rock do have an effect on the level of enrichment of particular elements in this narrow

alteration zone. The elemental trends mimic those of the fissure fill material mentioned

previously. The isocon diagrams also reveal that the concentrations of typically immobile

elements like Zr, REE, and Nb are diluted by the introduction of silica near the fissures (Fig 9).

Chemical characteristics of sulfides in fissures

The major and trace element composition of sulfides—particularly pyrite—has proven to

be a useful tool when determining the source, controls, and timing of a variety of sulfide-hosted

ores (Cook et al., 2009a; Large et al., 2009; Cook et al., 2016; Dubosq et al., 2018; Sykora et al.,

2018; Wu et al., 2018). Pyrite is ubiquitous in several types of deposits, and is the major host of

Au in Carlin-type deposits (Palenik et al., 2004; Reich et al., 2005; Large et al., 2009), orogenic

gold deposits (Reich et al., 2005; Large et al., 2009; Zhang et al., 2017; Wu et al., 2018), and

may be the host for the Au in the distal disseminated deposits associated with Bingham

(Cunningham et al., 2004). It is also ubiquitous in each fissure regardless of location or host

rock, so it was a natural choice for more in-depth analyses. Other sulfide phases were also

investigated, but not in as much detail.

Pyrite compositional correlations mimic many of those noted in the whole rock

geochemistry of the fissure fill material since they are the bulk constituent. Those analyzed in the

Pb-Zn mineralization zone are enriched in many trace elements relative to those closer to the

center of the deposit. This enrichment is particularly evident for Ag, As, Au, Bi, Cd, Cu, Ni, Pb,

Sb, Sn, and Zn (Table 5). Similar trace element enrichments have been found in the transition zones from porphyry to epithermal environments of other porphyry Cu deposits (Maydagán et al., 2013; Sykora et al., 2018). Sykora et al. (2018) differentiate these pyrites into porphyry-stage and epithermal-stage based on textures, associated mineral assemblages, enriched trace element concentrations, and truncated trace element zonation patterns. They also add that overprinting where these two environments meet can create composite grains. Composite pyrite grains exist in Carlin-style and orogenic gold deposits as well, which are easily recognized by textures and chemical analysis (Cook et al., 2009a; Large et al., 2009; Dubosq et al., 2018).

Composite grains were not found in our samples based on textural evidence, SEM backscatter imaging, or EDS scans on an electron microprobe. Elemental distribution appeared uniform. This does not confirm that zonation does not exist, but more likely that the degree of zonation is not detectable by the methods mentioned previously. Very complex trace element zonation patterns have been recognized by more precise analyses such as element mapping by LA-ICP-MS (Large et al., 2009; Cook et al., 2016; Dubosq et al., 2018; Sykora et al., 2018; Wu et al., 2018). Only core and rim trace element analyses were performed in this study.

The pyrite from the epithermal environment has considerably higher concentrations of chalcophile trace elements compared to the pyrite from the porphyry environment (Fig. 10). The higher concentrations make the core-rim variations more obvious. If we consider only the grains that showed the highest concentration of trace elements, some generalizations can be made: Ag, Cd, Cu, Ni, Sb, Sn, and Zn are typically more enriched in the cores, while As and Au are typically more enriched in the rims. This is a different variety of composite grains than described by Sykora et al. (2018) where porphyry-stage pyrite is overprinted by epithermal-stage
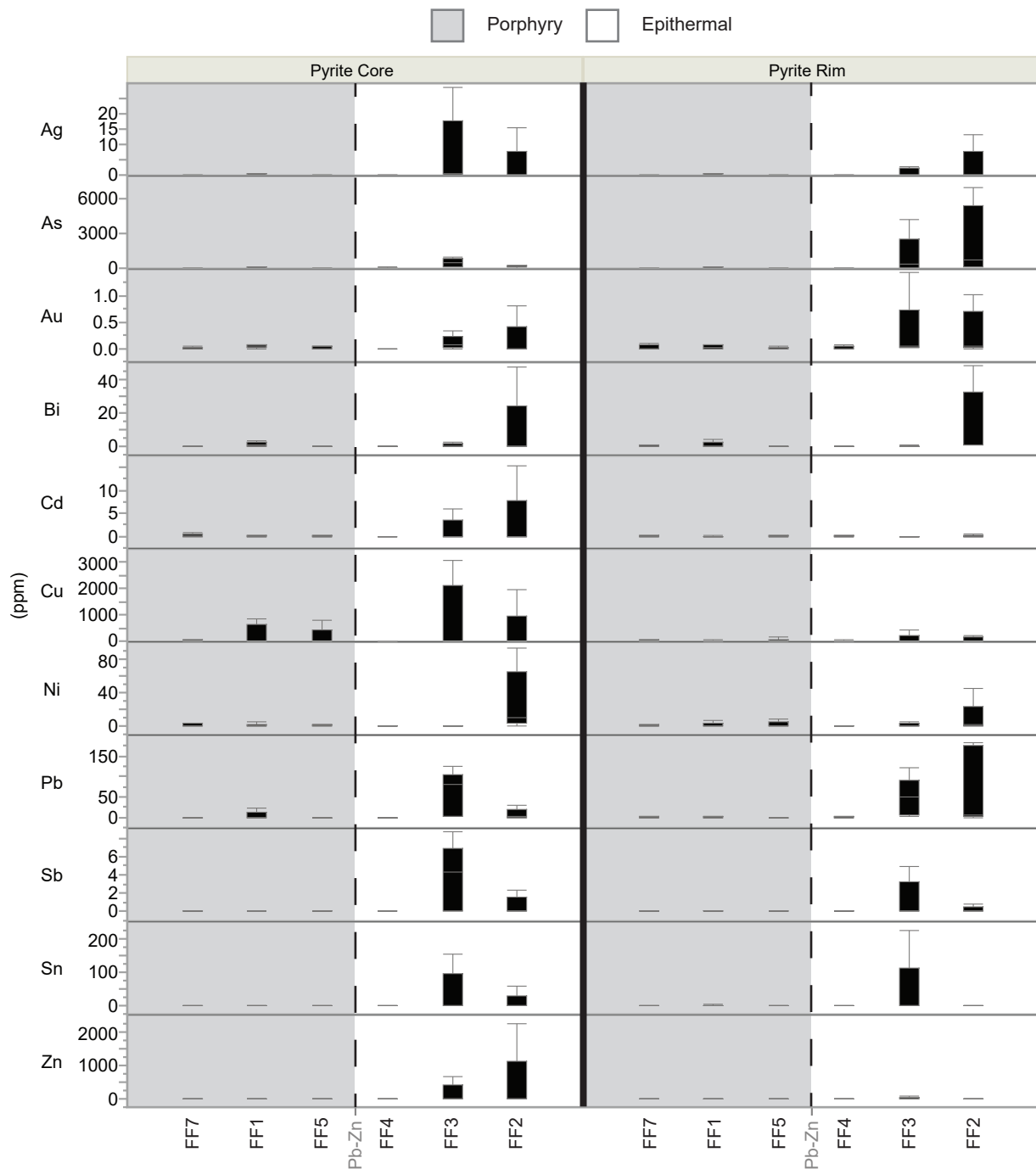
Fig. 10. Core and rim trace element concentrations in pyrite grains (n=60) from both sides of the Pb-Zn boundary in Fig. 2, which is illustrated here by the grey dashed line. The bottom and top of each plotted box reflects the 1st and 3rd quartile, respectively. Values outside of the interquartile range are plotted as whiskers. Fissures are ordered from left to right by increasing distance from the center of the deposit. Pyrite grains in the outer epithermal environment (FF3, and FF2) show obvious enrichments in these trace elements relative to those from the porphyry environment (FF7, FF1, FF5).

Table 5. Select major and trace element compositions of pyrite from fissure fill material.

Grain		Porphyry						Epithermal					
		FF1-3	FF1-3	FF5-3	FF5-3	FF7-1	FF7-1	FF2-1	FF2-1	FF3-3	FF3-3	FF4-2	FF4-2
Host Rock		QZ	QZ	MZ	MZ	MZ	MZ	MZ	MZ	LS	LS	QZ	QZ
Location		Core	Rim	Core	Rim	Core	Rim	Core	Rim	Core	Rim	Core	Rim
Fe	wt%	46.20	46.53	46.90	46.13	46.71	46.39	45.45	45.68	46.31	46.38	46.60	46.36
S	wt%	54.01	54.07	52.98	53.45	53.45	53.59	54.05	53.82	53.35	52.84	54.09	53.69
Ag	ppm	mdl	mdl	mdl	mdl	mdl	mdl	16	13	mdl	2.8	mdl	mdl
As	ppm	27	1.9	mdl	mdl	mdl	mdl	270	7100	100	4200	8.4	2.8
Au	ppm	mdl	mdl	mdl	mdl	mdl	mdl	0.8	1.0	mdl	1.5	mdl	mdl
Bi	ppm	3	1.2	mdl	0.3	mdl	1.0	48	48	0.1	0.4	mdl	0.4
Co	ppm	1.7	16	4.2	9.7	1.4	0.7	mdl	mdl	mdl	2.2	0.4	0.6
Cr	ppm	2	mdl	mdl	5	mdl	3	mdl	mdl	2	3	mdl	mdl
Cu	ppm	5	28	20	2.7	73	62	2000	140	2.0	23	mdl	40
Mn	ppm	1.8	2.1	2.3	2.3	2.3	2.9	4.1	mdl	1.7	2.0	1.4	1.7
Ni	ppm	mdl	6	1.2	8	mdl	2.1	mdl	mdl	mdl	5	mdl	mdl
Pb	ppm	24	1.7	mdl	mdl	mdl	1.3	30	170	4	52	0.2	2
Sb	ppm	mdl	mdl	mdl	mdl	mdl	mdl	2.4	mdl	mdl	4.9	mdl	mdl
Se	ppm	36	30	70	60	170	100	80	40	3	12	mdl	5
Sn	ppm	0.7	4	0.6	0.4	mdl	0.7	60	1.0	mdl	0.8	mdl	mdl
Te	ppm	50	0.9	mdl	mdl	mdl	4	mdl	13	mdl	2.8	0.2	2.3
Zn	ppm	0.6	0.5	mdl	1.4	mdl	1.8	2270	3	1.6	0.4	mdl	mdl

Notes: Major elements were determined by EMPA and trace elements were determined by LA-ICP-MS; concentrations below detection limits are reported as mdl

pyrite because only a few trace elements (As and Au) were enriched in the rims rather than a general enrichment of chalcophile trace elements.

Concentrations of Cu and As range from sub-ppm to several 1000 ppm in the epithermal pyrite. They show a negative correlation with one another when either one reaches concentrations in the 1000s of ppm. The decoupling of Cu and As in pyrite has been observed in several types of deposits (Tanner et al., 2016; Tardani et al., 2017), including porphyry Cu deposits (Reich et al., 2013), and is associated with changes in the composition of the mineralizing fluids (Reich et al., 2013; Tardani et al., 2017). Pačevski et al. (2008) determined that as much as 8 wt% Cu can be structurally bound in hydrothermal pyrite; here concentrations are much lower and reach only as high as 0.31 wt%. More recent observations reveal the significance of nano-sized chalcopyrite inclusions in pyrite—<1 μm—which contribute to Cu enrichment in addition to solid solution (Reich et al., 2013; Tardani et al., 2017).

In some ore deposits, gold forms as nanoparticles in As-rich rims of pyrite, especially in Carlin-type deposits (Palenik et al., 2004; Reich et al., 2005). Reich et al. (2005) determined that in Carlin-type and epithermal deposits, the Au in pyrite only occurs as nanoparticles, as opposed to solid solution, when the Au:As ratio is greater than 0.02. The average Au:As ratio from Au-bearing pyrite in our samples is significantly lower—0.001. This suggests that Au is likely present as solid solution rather than nanoparticles in the fissure pyrite. High Au concentrations have also been found in As-free pyrite in the form of telluride inclusions in other deposits (Cook et al., 2009a), but the single telluride micro inclusion that was found did not contain Au based on EDS (>2 wt%).

Despite the presence of Au in the pyrite, it alone cannot be the source of Au in the fissure ores based on simple mass balance calculations. The highest whole rock Au concentration from

our sample set was 4.6 ppm, while the highest Au concentration in the pyrite from that same sample was only 1.0 ppm. The modal percent of pyrite in the sample was approximately 80%, which is fairly representative of most of the fissures. Even if we assume that every pyrite grain had 1.0 ppm Au, it could only account for 18% of the total Au in the rock. This indicates that another mineral phase supplies the majority of the Au in the ore with several 10s of ppm Au. Alternatively, our selection for laser ablation analyses of "clean" locations free of inclusions and cracks, may have introduced an inherent bias. Gold has been found in some cases to be preferentially located along healed fractures or in micro inclusions in Carlin and orogenic gold deposits (Cook et al., 2009a; Large et al., 2009), which would have been missed with our analytical methods.

Chalcopyrite typically had Au concentrations below detection limits (~0.4 ppm) apart from one grain with 3.1 ppm Au (Table 6). This same grain contained anomalously high values for Ag, As, and Pb suggesting a possible mineral inclusion that was not observed during grain inspections. Ignoring that outlier gives ore metal concentrations of 33.6 to 34.9 wt% Cu, 3.8 to 45 ppm Ag, and undetectable amounts of Au. George et al. (2018) found that hydrothermal chalcopyrite is not a preferential host for Au with maximum concentrations not usually exceeding a few ppm regardless of deposit type. The chalcopyrite compositions in the Bingham fissures confirm this finding. The chalcopyrite does host appreciable amounts of In, Mn, Se, Sn, and Zn with less Ag, As, Bi, Cd, Cr, Ga, Pb, and Sb (Table 6; Fig. 11). The trace element concentrations in chalcopyrite in the Bingham fissures are generally higher than in chalcopyrite from the potassic zones of other porphyry Cu deposits (Maydagán et al., 2013); for example, Zn can reach 1000s of ppm rather than only 100s of ppm. If this is also true for the main potassic ore zone chalcopyrite at Bingham, then it suggests that several sulfides, and not just pyrite, become
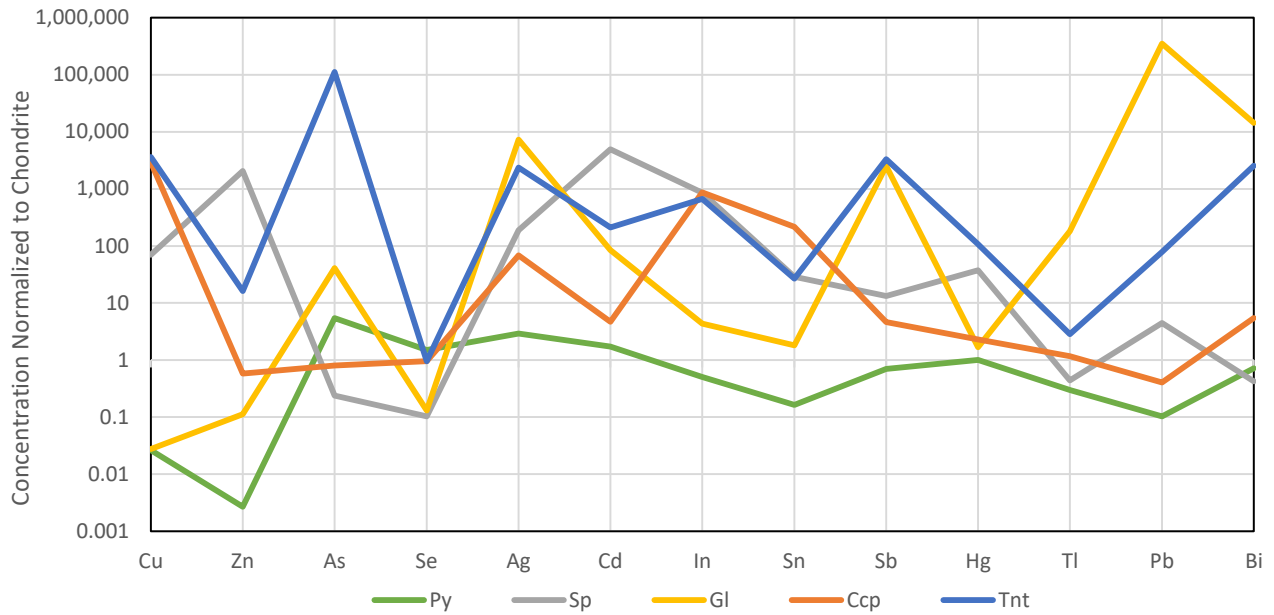
Fig. 11. Chondrite-normalized plot for select chalcophile elements in pyrite, sphalerite, galena, chalcopyrite, and tennantite from Bingham's fissure ore listed in order of atomic number. Chondrite values from McDonough and Sun (1995). Plotted values are based on median concentrations of elements in each mineral. For statistical purposes, all values below mdl were assumed to be mdl/2.

Table 6. Select major and trace element compositions of chalcopyrite from fissure fill material.

		Spot Anaylses					Veinlet Traverse				
Grain		FF2-CPY2	FF2-CPY3A	FF3-CPY1	FF5-CPY3A	FF5-CPY4	FF2-CPY4A	FF2-CPY4B	FF2-CPY4C	FF2-CPY4D	FF2-CPY4E
Host Rock		MZ	MZ	LS	MZ	MZ	MZ	MZ	MZ	MZ	MZ
Cu	wt%	34.19	33.79	34.04	34.77	33.90	33.91	34.34	34.18	34.41	34.40
Fe	wt%	30.32	30.44	30.21	27.71	30.54	30.53	30.66	30.35	30.38	30.25
S	wt%	35.13	34.79	35.09	35.01	34.64	35.29	35.36	35.09	34.97	34.86
Ag	ppm	3.8	13.7	mdl	980	mdl	8.4	9.3	35	9.5	11.8
As	ppm	mdl	15	mdl	8400	mdl	4	mdl	11	mdl	mdl
Au	ppm	mdl	mdl	mdl	3.1	mdl	mdl	mdl	mdl	mdl	mdl
Bi	ppm	0.4	1.7	mdl	1.9	0.5	0.6	0.4	mdl	mdl	1.3
Cd	ppm	12	mdl	mdl	mdl	mdl	mdl	20	22	17	12
Cr	ppm	mdl	30	5	9	8	mdl	mdl	11	mdl	3
Ga	ppm	mdl	7	mdl	mdl	mdl	mdl	mdl	mdl	5	9
Hg	ppm	mdl	mdl	mdl	1.5	mdl	mdl	mdl	mdl	mdl	mdl
In	ppm	46	87	108	mdl	1.9	76	69	64	64	61
Mn	ppm	23	mdl	14	9	mdl	14	18	32	39	12
Pb	ppm	1.7	3.4	6	130	mdl	1.2	1.0	3.0	1.0	1.0
Sb	ppm	mdl	8	mdl	8000	mdl	mdl	mdl	4	mdl	mdl
Se	ppm	50	20	20	40	130	30	10	40	10	50
Sn	ppm	97	400	330	2.0	380	219	128	105	270	560
Tl	ppm	mdl	mdl	mdl	73	mdl	mdl	mdl	mdl	mdl	mdl
Zn	ppm	4000	530	170	49	8	610	710	1600	660	560

Notes: Major elements were determined by EMPA and trace elements were determined by LA-ICP-MS; concentrations below detection limits are reported as mdl

more enriched in chalcophile trace elements with increasing distance from the fluid source and at cooler temperatures. The opposite has been suggested where chalcopyrite trace element abundances increase with crystallization temperature, or when co-crystallizing phases are absent based on analyses of chalcopyrite from several ore deposit types (George et al., 2016).

While it is evident that the chalcopyrite is late-stage, we can further constrain how the fluids evolved towards the waning stages by examining a traverse across a chalcopyrite veinlet from the center of fissure FF2. Five equally spaced spot analyses (Table 6; FF2-CPY4A through FF2-CPY4E) were done across the 3 mm chalcopyrite veinlet with the first and last analysis representing the edges of the veinlet. Bismuth, Ga, In, and Sn concentrations all decrease towards the center of the veinlet, while Ag, As, Cd, Cr, Mn, Pb, Sb, Se, and Zn all increase. These trends are replicated on both sides of the veinlet often with a two-fold difference between the edge and center concentrations. This further supports the previous observation that the concentration of chalcophile elements in chalcopyrite (and presumably other sulfides) increases at cooler temperatures, based on the assumption that the chalcopyrite in the middle of the veinlet crystallized later and a lower temperature than the edges. As mentioned previously, this could also be related to a reduction in the variety of sulfides over time, which would in turn allow chalcopyrite to host a wider variety of elements that would have otherwise have been incorporated into other sulfide phases.

Galena and sphalerite are examples of sulfides that can co-precipitate with chalcopyrite and affect its trace element incorporation (George et al., 2016). The Cd:Zn ratios in co-precipitated chalcopyrite and sphalerite can vary together, but should remain roughly equal between the two minerals when precipitating under similar physiochemical conditions from the same mineralizing fluid (George et al., 2018). Chalcopyrite from the fissures has an average

Cd:Zn ratio of 0.02, while the sphalerite has an average ratio of 0.006. This suggests that they did not co-precipitate, which is supported by chalcopyrite textures in thin sections indicating it formed later than the sphalerite. Our chalcopyrite analyses did not include micro inclusions of chalcopyrite in the sphalerite, such as those seen in Fig. 6b, as they were too small for LA-ICP-MS. If sufficiently large micro inclusions could be found, then the Cd:Zn ratios would be expected to be more similar in the chalcopyrite inclusions and sphalerite host. There has been an attempt to link Cd:Zn ratios in chalcopyrite to inferred crystallization temperatures (George et al., 2018), but it is not very well constrained and requires further development.

Sphalerite and galena grains were only large enough for LA-ICP-MS in sample FF3 hosted in limestone. Textural relationships strongly suggest co-crystallization as seen in Fig. 6h. Where possible, each grain was analyzed in two locations free of inclusions to determine homogeneity. These locations were typically close to the sphalerite-galena contact to also check for partitioning of trace elements between the two phases. Compared to all the other sulfides analyzed, the sphalerite grains are all very enriched in Mn and Cd (1000s of ppm), with moderate Ag, In, and Sn (10s-100s of ppm), with minor amounts of Cr, Ga, As, Se, Sb, Au, Hg, and Pb (<10 ppm to 10s of ppm) (Table 7; Fig. 11). The average Cu concentration is ~8,500 ppm, which is higher than the galena (max 140 ppm) and pyrite (max 3,100 ppm) and may be influenced by subsurface chalcopyrite inclusions not observed during grain inspections. However, sphalerite in other deposits are enriched in the same elements particularly Mn, Cu, and Cd, which are consistently in the 1000s of ppm (Palero-Fernández and Martín-Izard, 2005; Cook et al., 2009b). The preferential partitioning of Ga in sphalerite relative to the chalcopyrite and galena indicates a low temperature environment (George et al., 2016). The sphalerite grains do not appear to be homogenous in trace elements with concentrations between different spots on the same grain

Table 7. Major and trace element compositions of sphalerite from fissure FF3.

Grain		FF3-SPH1A	FF3-SPH1B	FF3-SPH2A	FF3-SPH2B	FF3-SPH3A	FF3-SPH3B	FF3-SPH4A	FF3-SPH4B
Host Rock		LS	LS	LS	LS	LS	LS	LS	LS
Zn	wt%	64.68	64.20	63.42	63.51	59.77	59.75	65.05	64.94
Fe	wt%	2.15	2.11	1.57	1.71	2.38	2.24	2.19	2.04
S	wt%	33.29	33.24	33.28	33.43	33.05	32.98	33.15	33.32
Ag	ppm	17	29	24	16	43	24	41	40
As	ppm	mdl	0.9	mdl	mdl	mdl	mdl	1.5	mdl
Au	ppm	mdl	mdl	0.20	mdl	0.21	mdl	0.27	0.23
Cd	ppm	3800	4280	3320	3680	3090	3160	3720	3200
Cr	ppm	1	4	3	3	4	3	4	2
Cu	ppm	3400	7300	8100	5200	15300	8700	8700	11000
Ga	ppm	11.1	64	15	41	11	2.5	6.3	8.4
Hg	ppm	14	11.4	13	12	9.0	10.0	11	11
In	ppm	63	31	74	18	170	255	41	149
Mn	ppm	720	690	1600	1660	1420	1450	1050	2000
Pb	ppm	7	9	13	3.6	70	7	41	50
Sb	ppm	1.3	5.1	1.1	1.0	2.4	mdl	4.0	2.4
Se	ppm	mdl	mdl	9	5	4	4	mdl	mdl
Sn	ppm	190	34	60	65	6	2.3	93	9

Notes: Major elements were determined by EMPA and trace elements were determined by LA-ICP-MS; concentrations below detection limits are reported as mdl

varying two to three fold in several cases suggesting significant trace element zonation, which occurs in other deposits as well (George et al., 2016). Sphalerite in fissure FF3 hosts appreciable amounts of Cu (3,400-15,300 ppm), but significantly less Ag (16-43 ppm) and even less Au (0.2-0.3 ppm, when detectable). Ragged ablation spectra for Ag, Pb, and Sb in sphalerite from other deposits have been attributed to nano-scale inclusions of sulfosalts (Cook et al., 2009b). In the sphalerite from FF3, Pb and Sb spectra show this raggedness to an extent, although both had typically low concentrations (average 25 ppm Pb and 2.5 ppm Sb) and so the variation could be analytical. Silver did not have such ragged signals, which leads us to believe the Ag concentrations reported here are representative of solid solution. This cannot be determined as confidently for Au, but the concentration (when detectable) was limited to a restricted range amongst different grains, which supports Au being in solid solution as well.

Galena in FF3 was most notably enriched in Ag, Bi, and Sb, with moderate amounts of As, Cd, Cu, Fe, Tl, and Zn, and lesser amounts of Au, Cr, In, Mn, Se, Sn and Te (Table 8; Fig. 11). Like sphalerite, galena shows similar enrichments of chalcophile trace elements as in several deposit types (George et al., 2015). High concentrations (up to 100s of ppm) of Hg and Ni have been found in galena from Pb-Zn vein deposits from the Alcudia Valley in Spain (Palero-Fernández and Martín-Izard, 2005), but neither was detectable in the fissure galena from Bingham. Comparison between the co-crystallized galena and sphalerite shows a clear partitioning of trace elements. Cadmium, Cu, Ga, Hg, In, Mn, Sb, and Sn show a preference for sphalerite while Ag, As, Bi, Sb, Te, and Tl show a preference for galena. While galena can host appreciable amounts of Ag, it is a poor host of Au and Cu. Concentrations of Ag in galena from FF3 range from 560-1,220 ppm, while Cu and Au were typically below detection limits.

Table 8. Major and trace element compositions of galena from fissure FF3.

Grain		FF3-GAL1	FF3-GAL2	FF3-GAL3A	FF3-GAL3B	FF3-GAL4A	FF3-GAL4B
Host Rock		LS	LS	LS	LS	LS	LS
Pb	wt%	86.36	86.52	86.65	86.57	86.59	86.27
S	wt%	13.43	13.48	13.54	13.57	13.54	13.49
Ag	ppm	1170	1220	750	560	970	1060
As	ppm	20	72	50	80	80	100
Au	ppm	mdl	mdl	mdl	mdl	mdl	0.3
Bi	ppm	1900	1980	16	18	1570	1560
Cd	ppm	68	58	63	62	44	44
Cr	ppm	mdl	mdl	3	1	6	6
Cu	ppm	mdl	mdl	140	90	mdl	mdl
Fe	ppm	mdl	mdl	700	mdl	mdl	300
In	ppm	0.3	mdl	0.4	0.5	mdl	0.4
Mn	ppm	6	3.5	mdl	4	mdl	mdl
Sb	ppm	370	308	820	590	263	330
Se	ppm	10	5	mdl	mdl	20	mdl
Sn	ppm	3	2	5	7	mdl	3
Te	ppm	13	14	15	20	15	19
Tl	ppm	25.2	25.7	23.2	22.2	25.9	27.0
Zn	ppm	40	mdl	50	50	mdl	30

Notes: Major elements were determined by EMPA and trace elements were determined by LA-ICP-MS; concentrations below detection limits are reported as mdl

Tennantite ($Cu_{12}As_4S_{13}$ or $Cu_6[Cu_4(Fe,Zn)_2]As_4S_{13}$) is the most complex mineral analyzed in this study as far as trace element incorporation is concerned. It has a highly variable formula and forms a solid solution series with tetrahedrite (($(Cu,Fe)_{12}Sb_4S_{13}$) (Miller and Craig, 1983) by substituting Cu for Fe and As for Sb. This undoubtedly results in a wider variety of trace elements that can be incorporated into its crystal structure. Tetrahederite-tennantite has been intensely studied and even referred to as the sulfide analog of amphiboles in terms of its potential usefulness in petrogenetic interpretation (Sack and Loucks, 1985). While tetrahedrite has been reported in fissure-hosted ores at Bingham during mine mapping, only tennantite was present in our samples.

Unlike the other sulfides, tennantite in FF2, FF3, and FF5 has variable major element composition in addition to trace elements (Table 9; Fig. 11). This is largely substitution of Zn and Fe, which have a strong negative correlation (r^2 = 0.94). However, zonation observable during BSE imaging (Fig. 12) has been attributed to As-Sb substitution (Maydagán et al., 2013). Simply attributing the fluctuating Zn and Fe concentrations to varying physiochemical conditions would not be appropriate as tennantite in fissure FF2 and FF5 has similarly low Zn:Fe ratios (averaging 0.20:1 and 0.01:1 respectively) despite being located at different distances from the center of the deposit (Fig. 2). Meanwhile, fissure FF3 was located at a similar distance as FF2 and has tennantite with significantly higher Zn:Fe ratios (average 8.51:1). We attribute this Zn-Fe fluctuation to the abundance of sphalerite, which is related to the host rock. Fissure FF2 and FF5 are both monzonite-hosted with Fe-rich tennantite and no observable sphalerite, while FF3 is limestone-hosted with Zn-rich tennantite and abundant sphalerite. Tennantite in FF3 is on the rims of some sphalerite grains in addition to chalcopyrite, which explains the higher Zn:Fe ratios.
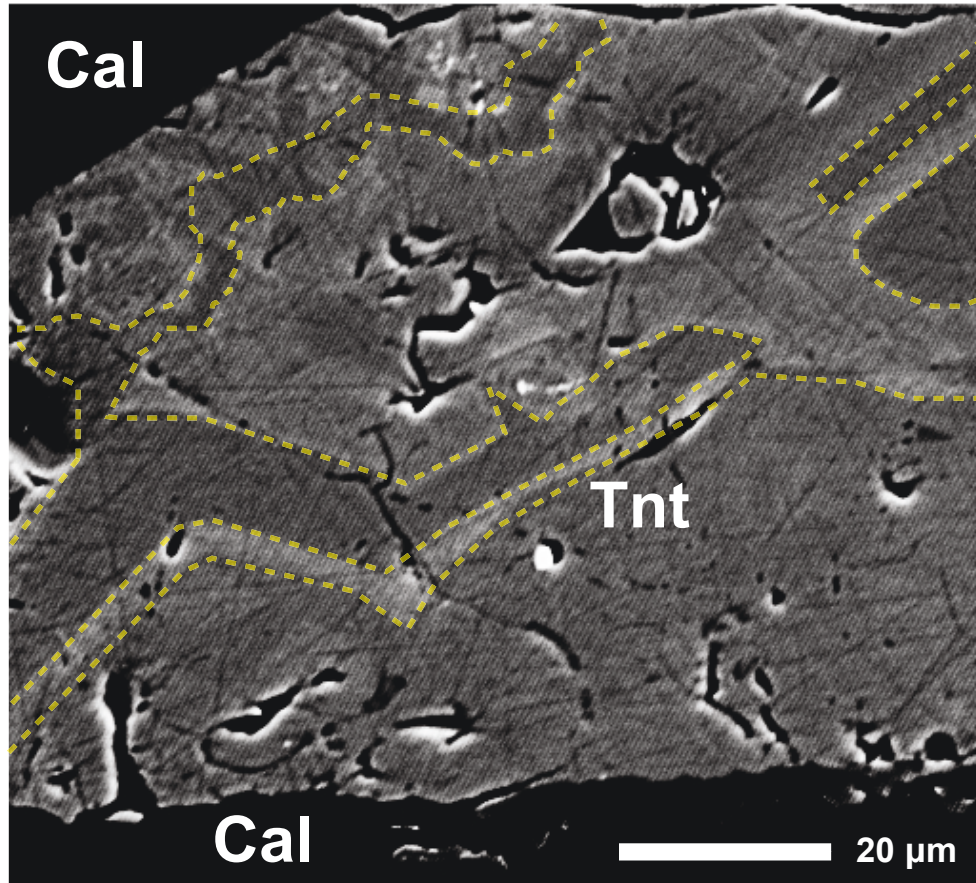
Fig. 12. BSE image of a tennantite (Tnt) grain from fissure FF5 with strong zonation outlined with dashed lines. This is most likely the result of Sb (bright zones) substituting for As (dark zones) (Maydagán et al., 2013), which commonly occurs in the tetrahedrite-tennantite solid solution series. The more ragged zonation closer to the top of the grain may be the result of dissolution, followed by regrowth of additional tennantite with more geometric zonation.

Table 9. Select major and trace element compositions of tennantite from fissure fill material.

Grain	FF2-TNT1	FF2-TNT2	FF2-TNT4	FF2-TNT5	FF3-TNT1A	FF3-TNT1B	FF3-TNT3	FF3-TNT4	FF5-TNT2	FF5-TNT3
Host Rock	MZ	MZ	MZ	MZ	LS	LS	LS	LS	MZ	MZ
Cu wt%	42.50	43.30	43.20	42.84	42.87	43.26	42.70	42.48	45.40	44.65
As wt%	20.78	21.19	21.48	20.98	20.53	19.94	20.65	20.75	20.39	19.78
S wt%	28.87	28.88	29.04	28.89	28.57	28.61	28.75	28.66	28.61	28.46
Zn wt%	0.82	2.51	mdl	mdl	7.98	7.73	7.19	7.53	0.05	mdl
Fe wt%	6.67	5.30	7.08	7.44	0.72	0.86	1.16	0.92	6.29	6.48
Ag ppm	7800	3050	3560	3780	330	730	280	450	350	600
Au ppm	mdl	mdl	mdl	mdl	mdl	1	mdl	mdl	1	3
Bi ppm	163	950	670	4400	400	350	84	900	340	410
Cd ppm	210	240	11	24	2200	2200	2100	2400	mdl	mdl
Cr ppm	mdl	3	8	10	mdl	11	3	mdl	4	6
Ga ppm	mdl	mdl	140	47	mdl	mdl	mdl	mdl	4	12
Hg ppm	24	22	230	140	33	35	26	35	21	20
In ppm	70	66	30	46	52	53	56	66	mdl	3
Mn ppm	162	54	1700	1460	1110	1120	1180	760	40	540
Pb ppm	114	87	3500	170	50	200	190	3000	60	2300
Sb ppm	170	600	3	4	18500	19800	7600	63000	400	1050
Se ppm	20	mdl	20	30	20	10	20	30	90	80
Sn ppm	166	140	145	76	5	4	30	mdl	49	330
Te ppm	15	mdl	17	16	10	21	10	1770	200	270
Tl ppm	mdl	mdl	4	1	mdl	mdl	1	0	129	1000
V ppm	mdl	mdl	mdl	mdl	mdl	mdl	mdl	4	mdl	2

Notes: Major elements were determined by EMPA and trace elements were determined by LA-ICP-MS; concentrations below detection limits are reported as mdl

In FF2 and FF5, tennantite was only found as a replacement product of chalcopyrite, resulting in lower Zn:Fe ratios.

The trace elements in tennantite (and textures) suggest that both sphalerite and chalcopyrite can be replaced by tennantite. The tennantite grains in the limestone-hosted fissure (FF3) typically had the highest Cd, Mn, and Sb while the grains in the monzonite-hosted fissures had the highest Sn (Table 9). Sphalerite in FF3 has 2-3 orders of magnitude higher Cd and Mn than chalcopyrite, while chalcopyrite has an order of magnitude higher Sn than sphalerite. The Sb may be higher in FF3 from galena inclusions, but is not typically above a few ppm in both sphalerite and chalcopyrite.

It is difficult to constrain which trace elements are most enriched in tennantite due to its high variability for a single element even within one sample. However, the most enriched elements are typically Ag, Bi, Cd, Mn and Sb, which are followed by moderate amounts of Hg, In, Pb, Se, Sn, Te and Tl, and lesser amounts of Au, Cr, Ga and V (Fig. 11; Table 9). Cadmium, Ga, In, Mn, Pb, Sn, Te, and Tl show 1-2 orders of magnitude higher concentrations compared to tennantite from other deposits (Maydagán et al., 2013; George et al., 2017). Elements highest in tennantite from the porphyry environment are Au, Se, Te, and Tl, while those highest in the epithermal environment are Ag, Bi, Cd, Hg, In, and Mn (Table 9).

While tennantite had more Au values above detection limits, it is also one of the least abundant minerals. Gold concentrations varied only from 1-3 ppm (when detectable), meaning it cannot be the primary Au host in these rocks which have up to 4.6 ppm Au. In contrast, tennantite can contribute significantly to Ag ore grades with concentrations in tennantite ranging from several 100 to several 1000 ppm (Table 9). Copper is fairly constant averaging 43.6±1.1

wt%, but its Cu contribution is still overshadowed by the more abundant chalcopyrite despite it having a lower Cu concentration (average 34.1±0.3 wt%).

These observations lead us to believe that Au must be texture-controlled (within fractures, as nano inclusions, etc.) as opposed to being preferentially incorporated as solid solution in a single mineral phase. Silver and Cu concentrations in whole rock analyses of the fissure fill material are more easily explained by the high concentrations found in the minerals analyzed (Ag in galena and tennantite; Cu in chalcopyrite, tennantite, and sphalerite). For example, the sulfide fill of FF3 had 511 ppm Ag and the average concentration of Ag in galena from that sample was 955 ppm. While all the minerals can contribute to the Ag content to an extent, galena alone can contribute all of the Ag if the modal abundance is 52%, which is a reasonable amount (Fig. 5d). Pyrite was considerably poorer in the ore metals apart from Cu, which reaches as high as a few 1000 ppm in some cases. Nonetheless, it likely remains the primary contributor of Au due to its overwhelming abundance in the transition zone from porphyry to epithermal mineralization. As mentioned previously, the modal abundance of pyrite decreases with increasing distance from the center of the deposit, which suggests Au may also decrease.

SULFUR AND OXYGEN ISOTOPES

Sulfur and oxygen isotope ratios are routinely analyzed in ore deposits and have long proven to be valuable in determining the source of mineralizing fluids (Rye and Ohmoto, 1974; Taylor, 1974; White, 1974). Isotope ratios were measured for quartz (for oxygen isotopes) and pyrite (for sulfur isotopes) from the fissure fill. The results are summarized in Table 10.

Sulfur Isotopes

The $\delta^{34}S$ values of pyrite are restricted to a very narrow range of 2.3-3.4‰. This is high compared to pyrite in many porphyry Cu deposits (Fig. 13), but is still consistent with a

Table 10. Oxygen and sulfur isotopes from fissure fill minerals.

Sample	Porphyry-Stage				Epithermal-Stage		
	FF1	FF5	FF7		FF2	FF3	FF4
$\delta^{18}O_{VSMOW}$ Quartz	12.0	13.1	14.0		-	11.9	11.5
$\delta^{34}S_{VDCT}$ Pyrite	2.9	2.3	2.7		2.8	2.7	3.4

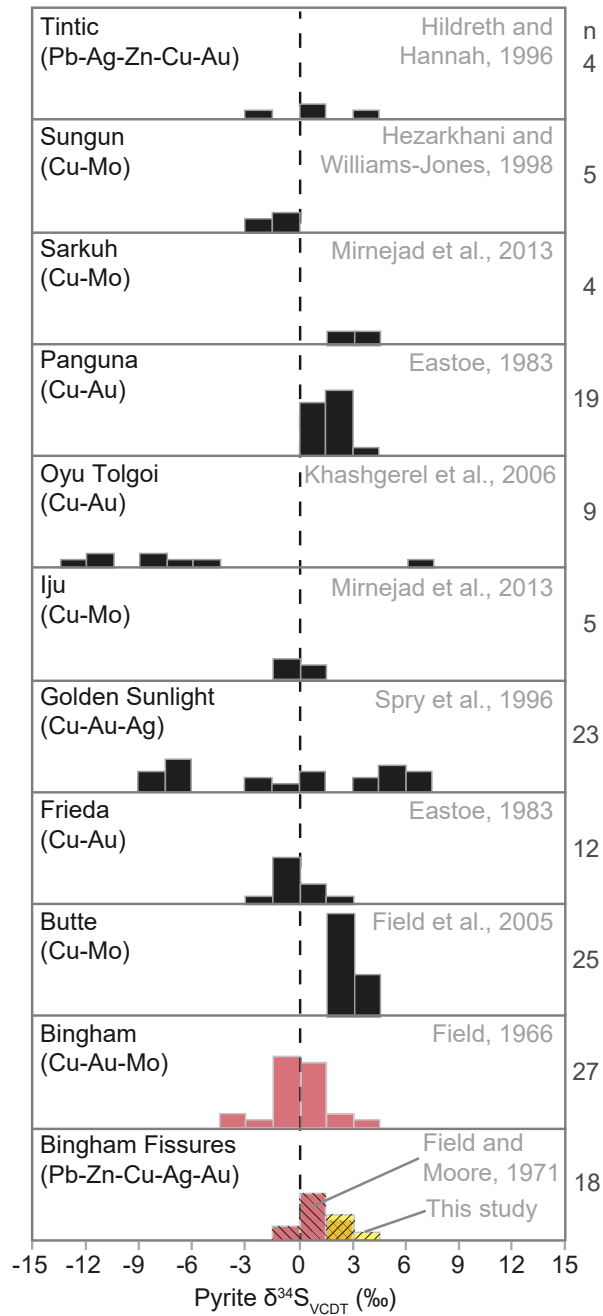Notes: Sample FF2 did not have sufficient quartz in fill material for isotope analysis

Fig. 13. Histograms of $\delta^{34}S$ in vein and disseminated pyrite from various porphyry Cu deposits and this study. $\delta^{34}S$ of pyrite from the fissures is somewhat higher than pyrite from across the deposit (Field, 1966) as well as pyrite from fissures more distal than our study area (Field and Moore, 1971). Nonetheless, the isotope signature is similar to many other deposits and is indicative of a magmatic source. A sedimentary-magmatic signature would result in a wide spread of values like the Golden Sunlight deposit (Spry et al., 1996). The Oyu Tolgoi deposit signature shows a spread as well, but has been attributed to oxidized and sulfate-rich fluids (Khashgerel et al., 2006).

magmatic source with typical values of 0±3‰ (Field et al., 2005). The $\delta^{34}S$ values of fissure pyrite fall within the upper range of pyrite values at Bingham reported by Field (1966), which range from -3.9 to 3.4‰. A later study by Field and Moore (1971) focused specifically on the fissures and found consistently positive $\delta^{34}S$ values for vein pyrite (average 1.6‰, range 0.4-3.8‰), which decreased with increasing altitude. The latter trend was not observed in our samples, although this may be due to the limited range of elevations (from 1902 m to 2115 m).

The $\delta^{34}S$ values from the fissure pyrites, and their narrow range, align particularly well with pyrites from the Butte (average 2.7±0.6‰) and Sarkuh (average 2.9±0.3‰) porphyry copper deposits (Field et al., 2005; Mirnejad et al., 2013). The Butte and Sarkuh $\delta^{34}S_{pyrite}$ values have been explained by the incorporation of sedimentary rocks with high ^{34}S into the magmatic source of the mineralizing fluids (Field et al., 2005; Mirnejad et al., 2013). The $\delta^{34}S$ values of fissure pyrite also overlap with pyrite from mineralized fissures in the younger East Tintic mining district just south of Bingham—the source of which is believed to be a late unexposed intrusion at depth (Hildreth and Hannah, 1996).

Oxygen Isotopes

The $\delta^{18}O$ values of quartz from the fissures are more puzzling. They are very enriched in ^{18}O compared to other porphyry Cu deposits and show a much broader range (Fig. 14), with a mean value of 12.5±0.9‰. They are also higher than vein quartz from Bingham reported by Bowman et al. (1987), which have a mean value of 9.1 ±0.6‰ (range 8.3-10.4‰) and become higher with increasing distance from the center of the deposit (r^2=0.53). The fissure sample locations in our study begin roughly where the vein quartz samples from Bowman et al. (1987) ended, and continue farther away from the center of the deposit. They continue to increase in $\delta^{18}O$ values continuing the trend of ^{18}O enrichment with increasing distance.
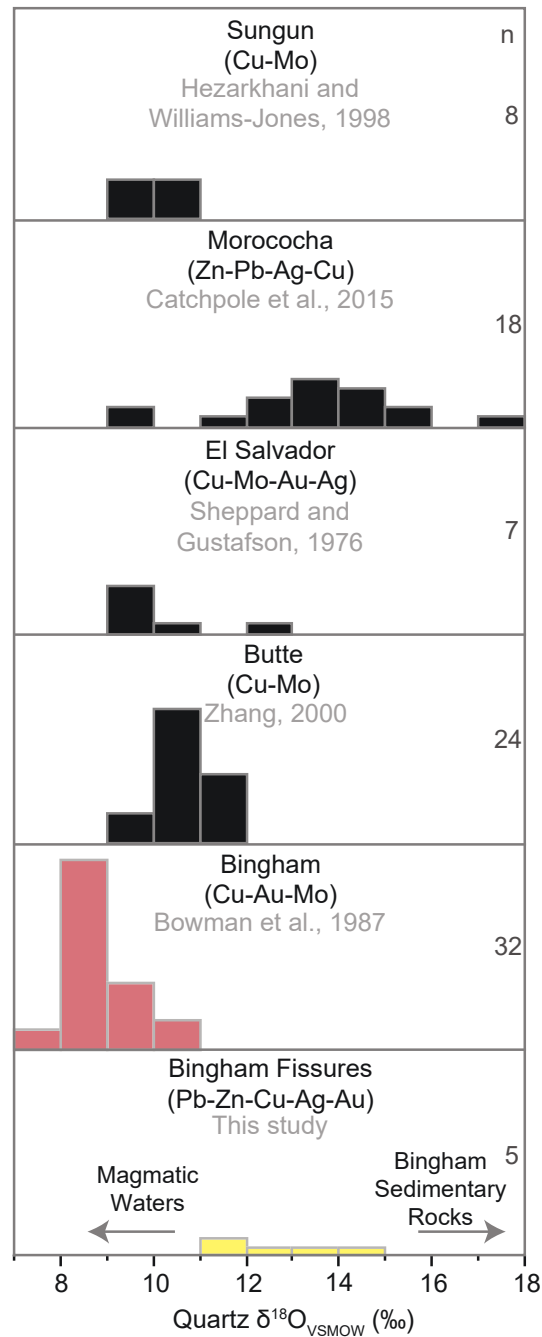
Fig. 14. Histograms of $\delta^{18}O$ for vein quartz from various porphyry Cu deposits. The quartz from the Bingham fissures has a wider spread and somewhat higher values than quartz analyzed in past studies at Bingham (Bowman et al., 1987). The fissure-filling quartz aligns more closely with quartz from porphyry-related base metal veins of the Morochoca District in Peru (Catchpole et al., 2015). At Bingham, this appears to be the result of increased fractionation at lower temperatures.

The $\delta^{18}O$ values of quartz in fissure veins are similar to those from the porphyry-related base metal veins in the Morococha mining district in Peru (13.4±1.9‰) (Catchpole et al., 2015). This is explained by the assimilation of a significant portion of high ^{18}O crustal rocks in the magmatic source of the mineralizing fluids (Catchpole et al., 2015).

DISCUSSION

All of the data and observations presented here provide constraints on the origin, timing, and controls of mineralization. They also provide valuable information that could be used for more efficient mining and processing of the fissure ore at Bingham.

Structural constraints on the origin and age of mineralized fissures

The abundance of joints, fractures, and faults in the Bingham deposit make even relative structural dating difficult. An in-depth structural analysis of the deposit is well beyond the scope of this study, and will not be attempted. However, some definitive observations constrain the timing of fissure formation. In the south side of the deposit, the mineralized fissures cut all of the intrusive and sedimentary units, other structures (folds, faults, joints), and alteration halos (potassic and propylitic) and thus appear to be the youngest structures (Fig. 2). In the north side of the deposit, weakly mineralized fissures with the same trend also cut all igneous rock units including the quartz latite porphyry, which is the youngest intrusive unit (Fig. 2). Small (<5 m wide) monzonite dikes in our study area (particularly in the Quartzite Xenolith) parallel fissure orientation indicating that they are coeval with fissure-oriented joints. This is supported by the strong propylitic alteration along these same joints, which confines their formation to before the mineralization and hydrothermal activity associated with the quartz monzonite porphyry. Early intrusion of monzonite coupled with the regional stress field may have helped formed these joints creating preferential pathways for hydrothermal fluid flow. The fissures cut all igneous units and indicates that the stress regime was similar at least from the time of monzonite (MZ)

intrusion until after the final quartz latite porphyry (QLP) dikes. On the other hand, it has been proposed that a dynamic stress regime fluctuated between orthogonal orientations repeatedly and allowed for the emplacement of the intrusions at Bingham (Gruen et al., 2010; Kloppenburg et al., 2010). It is quite likely that local stress fields formed and changed in response to the sequentially emplaced intrusions, but the consistency of distal dike and mineralized fissure orientations (NE; Figs. 2 and 3) across the entire deposit suggests they were controlled by a consistent, long-lived regional stress field. The orientation of the NE-trending fissures is not unique to the Bingham deposit. They are remarkably similar to the NE-striking mineralized fissures, pebble dikes, and andesite dikes of the early-Oligocene East Tintic mining district 70 km to the south (Hildreth and Hannah, 1996; McKean et al., 2011). They also share similar NE-trends with micro fractures, joints, and dikes associated with various late-Eocene to early-Oligocene plutons in northern Utah and Nevada (Ren et al., 1989; Kowallis et al., 1995). This indicates that while the intrusions were responsible for the formation of these structures—including the Bingham fissures—a far field stress was responsible for their NE orientation.

Source of mineralizing fluids

The source of fissure mineralization is most intuitively linked to the same fluids that formed the main Cu-Au-Mo ore body at Bingham. However, this becomes less evident when we consider the S and O isotope ratios reported here, as well as the observation that the fissures on the south side of the deposit are more abundant, wider and more heavily mineralized than those on the north side.

As noted previously, assimilation of crustal material has been used to explain high $\delta^{18}O$ values in quartz and high $\delta^{34}S$ values in sulfides at other porphyry deposits (Field et al., 2005; Mirnejad et al., 2013; Catchpole et al., 2015). This does not seem to adequately explain the elevated isotope ratios in the fissure quartz and pyrite since those same minerals in other

locations of the deposit have expected values for a magmatic source (Figs. 13 and 14). An alternative method was proposed by Cunningham et al. (2004) to explain the elevated $\delta^{18}O$ values in hydrothermal fluids on the north side of the deposit. They called on the involvement of high ^{18}O water formed in an evaporating crater lake at the summit of the Bingham stratovolcano that drained as groundwater in the mineralizing system. This theory presents several challenges, but nonetheless indicates that the need for elevated ^{18}O hydrothermal fluids is not unique to the south side of the deposit.

Another explanation for the anomalous isotope ratios is the fluids originated from an unexposed pluton similar to the source of fissure mineralization in the East Tintic mining district (Hildreth and Hannah, 1996). It is plausible that a younger pluton with slightly heavier S and O isotope values intruded beneath the south end of the deposit. This could have further dilated pre-existing NE-trending fissures and provided a source of localized mineralization. This explanation is unlikely as the mineral assemblages, mineral compositions, and whole rock geochemistry vary systematically from the center of the deposit and are consistent with cooling of hydrothermal fluids along that path. A separate late-stage intrusion would surely result in anomalous overprinting that would disrupt these systematic patterns, such as the Pb-Zn mineralization distal to the center of the deposit.

The high $\delta^{18}O$ values from the fissure quartz could also result from magmatic water mixing with meteoric water enriched in ^{18}O. This is contrary to what would normally be expected as meteoric waters are generally depleted in ^{18}O relative to magmatic water (Li et al., 2017). However, if the meteoric water equilibrated or exchanged with high ^{18}O sedimentary rocks, then this explanation is plausible. Enrichment of ^{18}O in hydrothermal quartz occurs in late-stage sericitic veins at the Ann-Mason (Nevada) porphyry Cu deposit as well, which was

explained by a large component of ^{18}O-enriched meteoric water or seawater (Dilles et al., 1992). Seawater would have been unlikely at Bingham, though it is plausible that briny formation waters existed prior to the formation of the deposit (Bowman et al., 1987) and mixed with the magmatic fluids that precipitated quartz.

The quartzite and carbonate rocks on the north side of the deposit have δ^{18}O values as high as 18.6 and 29.8 per mil, respectively (Cunningham et al., 2004). At the time of intrusion, meteoric water would be heated and begin to convect through these sedimentary rocks. This would allow effective transfer of ^{18}O from the rocks to the meteoric water. The result would be depletion of ^{18}O in the wall rocks closest to the deposit. In fact, Cunningham et al. (2004) found ^{18}O in the sedimentary rocks was lowest near the deposit and increased with distance, which aligns with this theory. With increasing distance from the deposit, these high ^{18}O exchanged meteoric waters could dominate and mix with pulses of lower ^{18}O magmatic fluid. Quartz crystallizing from this mixed hydrothermal fluid would then contain elevated ^{18}O values relative to magmatic quartz, or hydrothermal quartz closer to the deposit center.

The second and third generation of quartz found by textural analysis (Fig. 6e) and SEM-CL imaging (Fig. 7) were probably incorporated in our bulk separates and implies that the δ^{18}O values reported here are a composite of the two. The first generation of quartz near the selvages was likely missed since samples were trimmed where the sulfides ended to avoid any possible wall rock contamination. If the high δ^{18}O values in quartz are the result of magmatic water mixing with high ^{18}O meteoric water, then the δ^{18}O values could increase with time as the fluid continued to exchange oxygen with the wall rocks. The highest δ^{18}O values would then be in the third generation of quartz—which dominates the fissures. Li et al. (2017) have shown how in-situ O isotopes in hydrothermal quartz can record pulses of magmatic fluids followed by an

influx of (low or high ^{18}O) meteoric water after each pulse. This technique could be applied to the three generations of quartz found in the fissures in order to determine hydrothermal fluid evolution with time and which generation of quartz has higher $\delta^{18}O$ values

A final explanation for the anomalous isotope ratios may simply be stronger isotope fractionation due to low temperature fluids, which is acknowledged by Field et al. (2005) and Tanner et al. (2016) for other porphyry deposits. We suggest this is the primary reason for the higher isotope ratios, though some of the mechanisms mentioned previously could have enhanced it. Evidence for low temperatures in the late stage of fissure mineralization includes: marcasite found within chalcopyrite veinlets (Fig. 6i), fine-grained quartz veinlets (Fig. 6e), and dull luminescence of that same quartz (Fig. 7). Hydrothermal marcasite does not typically precipitate at temperatures >240°C (Murowchick and Barnes, 1986), which indicates that the fluids during chalcopyrite precipitation reached this low. The brightness of quartz observed during SEM-CL imaging has been linked to Ti contents and higher crystallization temperatures (Wark and Watson, 2006) meaning dull luminescence in quartz suggests cooler temperatures. Further temperature constraints come from the mineral assemblage of pyrite, chalcopyrite, galena, sphalerite, tennantite (+tetrahedrite), which indicates temperatures <300°C and an intermediate-sulfidation environment (Einaudi et al., 2003; Maydagán et al., 2013). Oxygen isotope fractionation equations of Sharp et al. (2016) result in an increase of 3.5‰ in quartz from the same water when it drops from 350°C to 250°C. Adding 3.5‰ to the $\delta^{18}O$ values in Bowman et al. (1987) would explain those found in the fissures without a need for a more complicated process.

Sequence of formation and mineralization

Late-stage Pb-Zn veins and halos are typical of several porphyry Cu deposits and related to porphyry mineralization (Einaudi et al., 2003; Sillitoe, 2010). Our observations do not suggest

the need for an alternative explanation for the Bingham fissures. Catchpole et al. (2015) demonstrated through detailed fluid inclusion studies that base metal mineralization can form from the same fluids responsible for porphyry mineralization. The proposed model for the formation of the fissures and their associated mineralization is outlined below and incorporates this concept along with observations from this and past studies (Figs. 15 and 16). The model must explain the origin of the mineralizing fluids, preferred orientation of the fissures, sequence of mineralization, metal zonation, S and O isotope signatures, crosscutting relationships of mineralization, alteration, and faulting, and observations already documented by other workers.

The equigranular monzonite was the first to intrude. Overpressure of the larger magma chamber below caused the roof of the intrusion to bulge as it was emplaced resulting in high-angle radial extension and fracturing (Gruen et al., 2010). Steep radial fractures are common closer to intrusions, but with increasing distance, they tend to reorient and align with the regional stress field (Boutwell, 1905; Muller and Pollard, 1977; Dilles and Einaudi, 1992; Hildreth and Hannah, 1996; Cammans, 2015). The orientations of the mineralized fissures are a representation of this phenomenon, having formed as joints at this time with their orientation controlled by far-field stress as discussed previously (Fig. 16). Thin (<5m wide) monzonite dikes parallel these NE-striking joints and appear to have formed at the same time (Fig. 15b).

The intrusion of the dike-like quartz monzonite porphyry followed and produced the Cu-Au mineralization in the main central ore body (Fig. 16) (Gruen et al., 2010; Porter et al., 2012; Seo et al., 2012). Fluid pressure build-up caused the roof to bulge again (Gruen et al., 2010), and dilated both the existing joints in the main ore body and the more distal fissures (Fig. 15c) as evidenced by propylitic alteration that fills the joints. The dilation could have caused the fissures to propagate farther out. This process of dilation and propagation continued to varying degrees
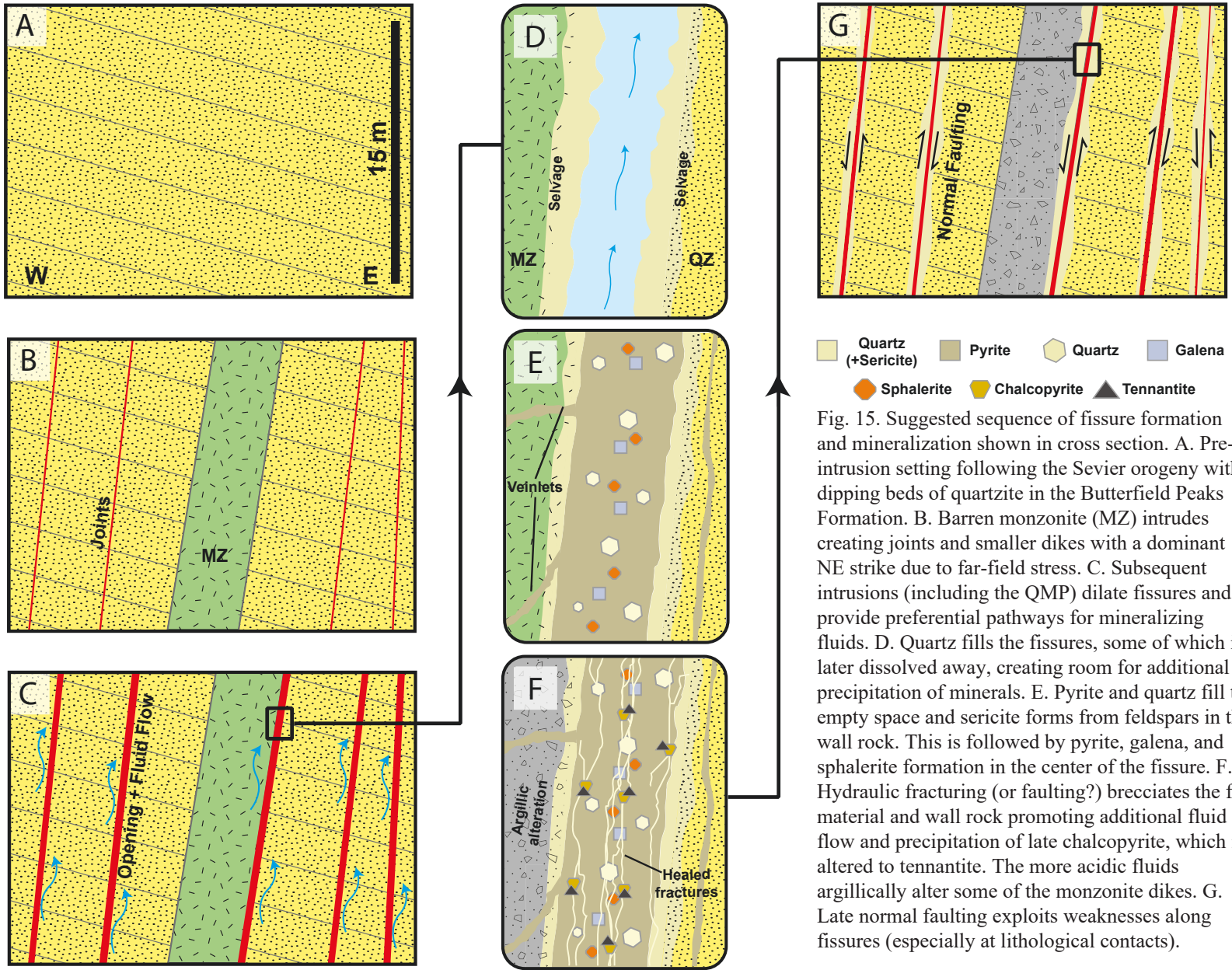
Fig. 15. Suggested sequence of fissure formation and mineralization shown in cross section. A. Pre-intrusion setting following the Sevier orogeny with dipping beds of quartzite in the Butterfield Peaks Formation. B. Barren monzonite (MZ) intrudes creating joints and smaller dikes with a dominant NE strike due to far-field stress. C. Subsequent intrusions (including the QMP) dilate fissures and provide preferential pathways for mineralizing fluids. D. Quartz fills the fissures, some of which is later dissolved away, creating room for additional precipitation of minerals. E. Pyrite and quartz fill the empty space and sericite forms from feldspars in the wall rock. This is followed by pyrite, galena, and sphalerite formation in the center of the fissure. F. Hydraulic fracturing (or faulting?) brecciates the fill material and wall rock promoting additional fluid flow and precipitation of late chalcopyrite, which is altered to tennantite. The more acidic fluids argillically alter some of the monzonite dikes. G. Late normal faulting exploits weaknesses along fissures (especially at lithological contacts).

| Time (Ma) | 38.53 ——————→ 38.28 ——————————→ 38.13 →37.70 ————————————→ ? |

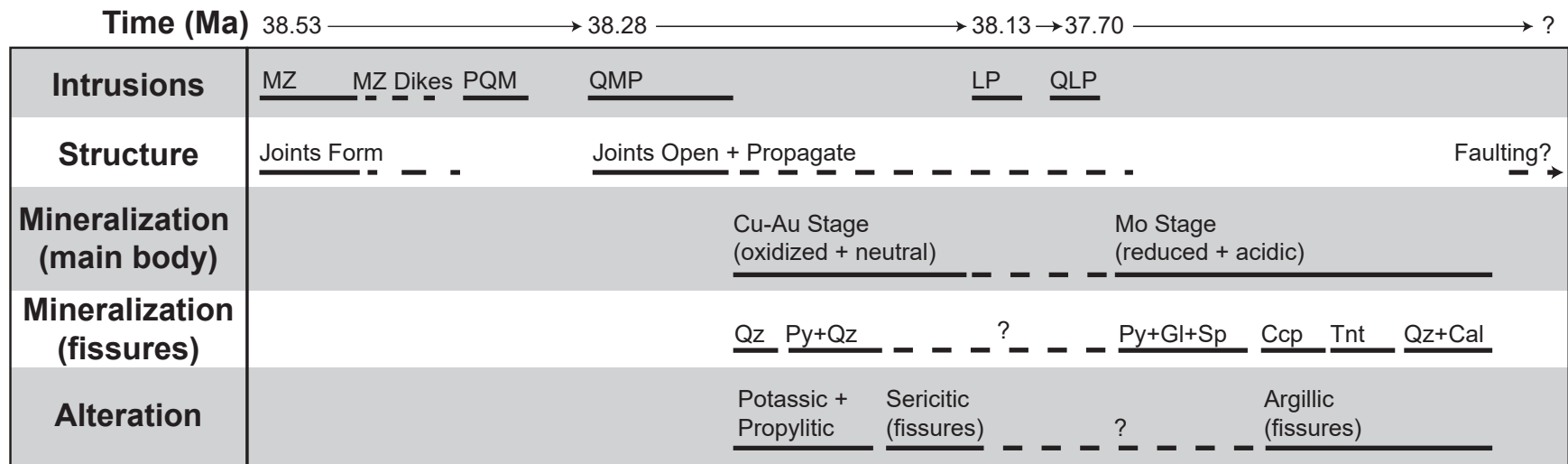|	
Intrusions	MZ MZ Dikes PQM QMP LP QLP
Structure	Joints Form Joints Open + Propagate Faulting?
Mineralization (main body)	Cu-Au Stage (oxidized + neutral) Mo Stage (reduced + acidic)
Mineralization (fissures)	Qz Py+Qz ? Py+Gl+Sp Ccp Tnt Qz+Cal
Alteration	Potassic + Propylitic Sericitic (fissures) ? Argillic (fissures)

Fig. 16. Timeline of events related to fissure formation as illustrated in Fig. 15 (time component not to scale). Dashed lines indicate episodic activity, or uncertainty if accompanied by a question mark. The formation, opening, and propagation of the NE joints related to the fissures is likely the result of both pressure-driven roof extension during intrusions (Gruen et al., 2010) and hydraulic fracturing by the mineralizing fluids. The relative timing and nature of the main ore body mineralization from Seo et al. (2012), and ages of intrusions from Large (2018).

throughout the emplacement of the intrusions. The hydrostatic pressure was released when joints in the center of the deposit and the more distal fissures dilated and magmatic Cu-Au mineralizing fluids were expelled. Quartz initially filled the stockwork veins in the main ore body, which was later partially dissolved away making room for late Cu-Fe sulfide precipitates and late quartz seen in SEM-CL imaging (Landtwing et al., 2005). The dissolved silica in the late fluids could then precipitate as the first generation of quartz in the fissure selvages accompanied by Fe-sulfide precipitation and sericitic alteration (Figs. 15d and 15e). The heavy Cu-Fe sulfide mineralization in the main ore body left only Fe-sulfide mineralization for the fissures in the form of pyrite. This was deposited at the same time as the second generation of quartz in the fissures. Early quartz-pyrite mineralization, as observed in the Bingham fissures, is a common feature of distal porphyry-related base metal veins (Einaudi et al., 2003).

The time between the early quartz and late Cu-Fe sulfides associated with the quartz monzonite porphyry is uncertain, although the estimated temperature of the fluids responsible for the Cu-Fe sulfides in the main ore body is 350-425°C (Landtwing et al., 2005). This is significantly lower than the temperatures associated with potassic alteration (~500-600°C) meaning the potassic alteration zone was already established. If the fissures were initially mineralized from the same fluids as the late Cu-Fe sulfide precipitation in the main ore body, then we can assume that the propylitic zone was also already established since the late sericitic alteration of the fissures cuts the propylitic zone. The temperature of this sericitic alteration was not determined, but temperatures as low as 175-250°C have been suggested at the Ann-Mason deposit, where late-stage sericitic quartz was also enriched in ^{18}O (Dilles et al., 1992). The first and second generation quartz in the Bingham fissures are zoned, which is oscillatory in the

second generation **(**Fig. 7) indicating temperature fluctuations. This occurred as pulses of magmatic fluid were progressively diluted by meteoric water at other deposits (Li et al., 2017).

The Pb-Zn mineralization clearly followed the quartz-pyrite-sericite mineralization based on the vein zonation (Figs. 5d and 15e). Base-metal veins have been associated with porphyry deposits rich in Mo (Einaudi et al., 2003); however, Seo et al. (2012) suggest that Mo precipitation at Bingham is late following the quartz latite porphyry since Mo veins cut both Cu-Fe sulfide veins and quartz latite porphyry dikes. While Catchpole et al. (2015) demonstrate that base metal veins can be derived from the same fluids involved with porphyry Cu-Mo mineralization, they do not consider this temporal component of late Mo precipitation. As such, we place Pb-Zn mineralization (galena+sphalerite+pyrite) after the quartz latite porphyry intrusion, while noting that more evidence is required to definitively constrain it to that time (Fig. 16).

Chalcopyrite and tennantite precipitation both followed Pb-Zn mineralization after intense brecciation caused by either tectonic faulting or hydraulic fracturing (Figs. 15f and 16). Both minerals are found in the third generation quartz veinlets that heal the fracture networks (Fig. 6j). The more acidic nature of the Mo-stage mineralizing fluids could have remobilized Cu from the main ore body (Seo et al., 2012), and transported it out to the fissures. Chalcopyrite filled interstitial space and formed small veinlets sometimes within the fractures of other sulfides, but also in the center of fissure fill material. Marcasite found in chalcopyrite veinlets in the fissures suggests a pH <5 (Murowchick and Barnes, 1986), which would explain why some of the monzonite dikes that parallel the fissures are argillically altered (Fig. 15f). The cooling of this fluid was apparently accompanied by an influx of meteoric water, which increased the fO_2 based on the replacement of chalcopyrite by late-stage tennantite (Fig. 17). If this meteoric water
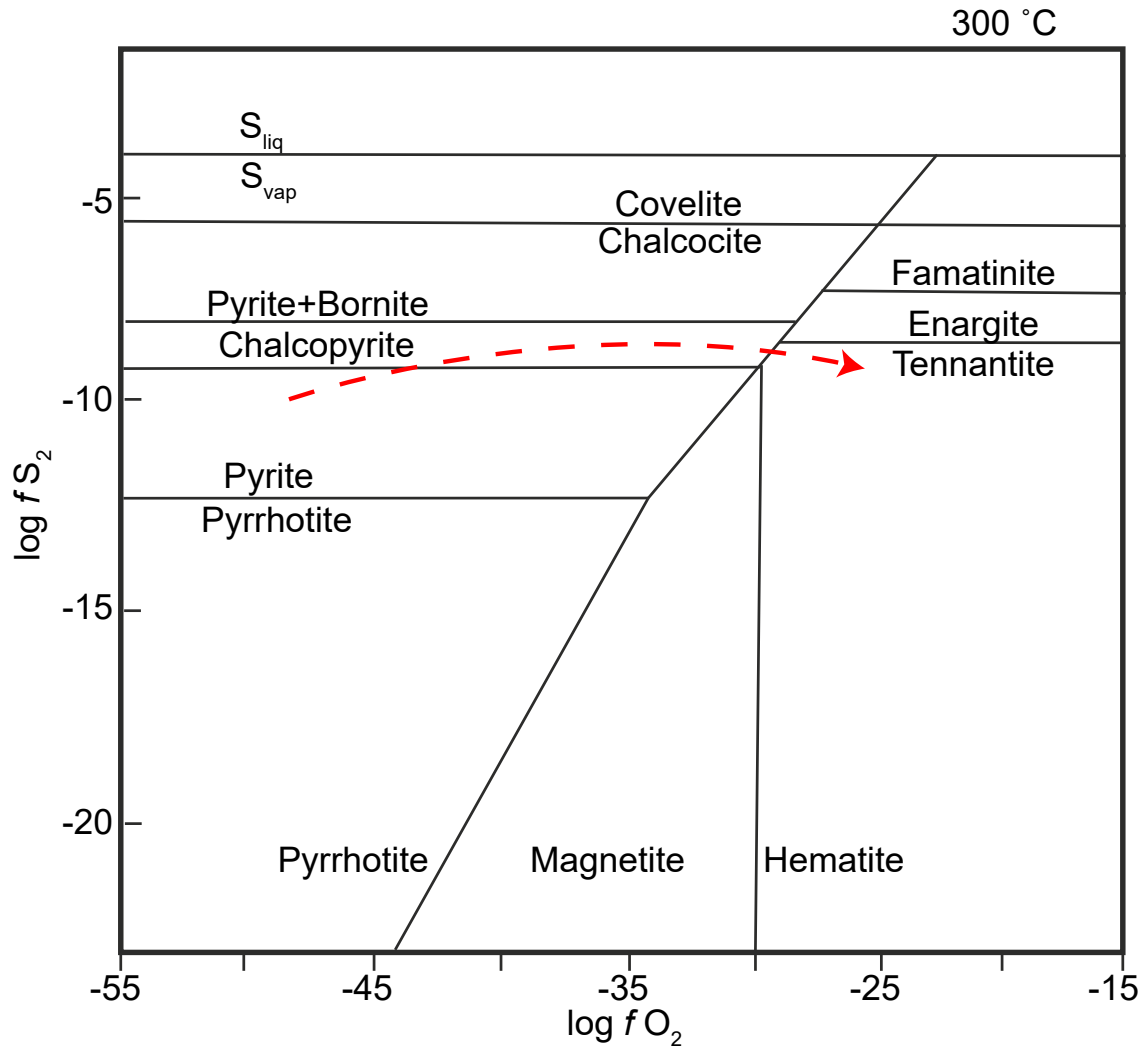
Fig. 17. S_2 vs O_2 fugacity diagram with stability fields for various Fe-Cu sulfides at 300°C modified from Maydagán et al. (2013). Pyrite was initially the only sulfide that precipitated, followed by galena and sphalerite. The fS_2 increased promoting chalcopyrite precipitation. Strong textural evidence suggests tennantite formed primarily by alteration of chalcopyrite (Fig. 6i, 6j). This requires a significant increase in fO_2 in the mineralizing fluids as shown with the red dashed line.

was enriched in ^{18}O, this would have resulted in the third generation quartz having higher $\delta^{18}O$ values.

The late appearance of Cu-Fe-As sulfosalts (enargite at high sulfidation states, and tennantite-tetrahedrite at intermediate sulfidation states) is common for both porphyry-related base metal veins (Catchpole et al., 2015), and intermediate- to high-sulfidation epithermal deposits (Einaudi et al., 2003). This is associated with an increase in sulfidation state (and acidity) over time as the mineralizing fluids cool and move upward in porphyry Cu systems (Sillitoe, 2010). Tennantite requires a lower sulfidation state than enargite (Fig. 17), which is indicative of an intermediate-epithermal environment; however, high-sulfidation epithermal systems can reach intermediate sulfidation states resulting in late gold-rich tennantite-tetrahedrite+pyrite (Einaudi et al., 2003). The consistently higher Au in late tennantite and higher Au concentrations on the rims of pyrite from the epithermal environment may be the result of a late overprint from a high-sulfidation epithermal environment. This could have occurred during the collapse of the hydrothermal system shifting the depositional environments inward.

Shearing and brecciation of the fissure veins occurred last associated with normal faulting that exploited the existing weakness of the fissures and altered wall rock (Fig. 15g). Faulting may have occurred during the creation of the fissures, but it definitively occurred after the deposition of the fissure fill material since the fault gouge is commonly made up of the sulfides pulverized to clay-sized particles.

Implications for mining and processing fissure ores

The whole rock analyses of the sulfide-rich ore show appreciable maximum values of Au (4.6 ppm), Ag (511 ppm), and Cu (2.3 wt%), so they can be ore-grade. However, the fissure ores are challenging to economically mine and process. The ore grade quickly diminishes to waste values typically within 1.5 m of a fissure with rapid dilution by barren wall rock (Fig. 9). Such a

66

significant structural control on ore is not ideal for open-pit operations where large shovel buckets exceed 6 m across. Narrow ore body widths explain why the fissures were initially mined exclusively underground.

The most advantageous areas would be associated with swarms of closely spaced fissures (Fig. 4e). A high concentration of fissures minimizes wall rock dilution. These swarms are not restricted to a single host-rock type, but appear to be more frequent in the quartzite, which has more brittle behavior relative to limestone or monzonite. The increased surface area from stronger brecciation of quartzite may also result in appreciable mineralization despite its overall lower reaction potential with mineralizing fluids. This shows that all of the major rocks types (limestone, monzonite, and quartzite) are capable of hosting fissure ore bodies large enough to mine and that they can be detected with blasthole assays if the analytical turnaround time is short enough.

However, the size of the area of fissure concentration is not the sole limiting factor. There also needs to be sufficiently high metal concentrations to offset dilution and to compensate for variable recovery rates. Recovery rates in downstream processing are related to the composition of the wall rocks. Both ore grade and recovery rates, along with several other proprietary variables, are included when determining the overall value of an ore block, which is calculated as a monetary value per ton of material. The highest ore grades of Au, Ag, and Cu are consistently found in the limestone fissures followed by monzonite and quartzite fissures when the data here are supplemented with mine assays. This is presumably related the greater reactivity potential of the limestone, which can reduce the pH of the mineralizing fluids promoting sulfide precipitation. However, the ore recovery rates (proprietary) are essentially the opposite with the quartzite-hosted ore showing the highest recovery due to its simple mineralogy, followed by the

monzonite ore, and finally the limestone ore. This means that quartzite fissure ore with low grades can be as economic to mine as a high-grade limestone ore, and should not necessarily be neglected. The monzonite ore fits in between these two end members with appreciable grades and recovery.

Fissure ore grades improve from the center of the deposit to the porphyry to epithermal transition zone, but are also accompanied by higher concentrations of deleterious elements (Table 3). This includes elements such as As, Bi, Ni, Pb, Sb, Se, Sn, Te, and Zn. These elements are able to persist through downstream processing and their elimination requires rigorous efforts to achieve desired purities for the mine's products. For example, Rio Tinto's target purity of silver bars at Bingham is 99.95%. Of the impurities, Bi cannot exceed 10 ppm. However, the host minerals of Ag in the fissures (galena and tennantite) can have Bi in the 1000s of ppm (Tables 8 and 9). Even if the majority of the Bi can be removed, there are environmental restrictions on the levels of Bi allowed in mine tailings. These impurities can also build-up on the furnace walls over time and be transported as fine particles along with SO_2 gas, leading to elevated emissions of heavily monitored elements like Pb. Limestone-hosted fissures have the most elevated concentrations of these elements, which can be orders of magnitude higher than proximal fissures hosted in other rock types. This is evident in both the whole rock and mineralogical compositions (Tables 3, 5). These problematic elements will presumably continue to increase in concentration as distal Pb-Zn mineralization begins to dominate the fissure ore extracted during subsequent expansion of the pit. This will likely require modifications to fissure ore processing, which could include changes to ore type blending, processing equipment, and flotation techniques.

CONCLUSIONS

Late, distal, base metal fissure ore at the Bingham Canyon porphyry copper deposit has long been recognized, but poorly studied despite its significance in the early stages of the mine's

development and resurgence in present-day expansion efforts. In-depth physical and chemical characterization of the fissures in the porphyry-epithermal transition zone provides insight into origin, timing, and controls of deposition. These findings also carry implications for mining and processing techniques of fissure ore, which may require modification from practices used in mining the main ore body.

The physical and chemical characteristics show many commonalities between all fissures, while several are controlled by the host rock and distance from the center of the deposit. Fissures are typically dominated by pyrite and multiple generations of quartz, with lesser amounts of other sulfides and gangue minerals. Associated alteration is predominantly sericitic, which cuts and is physically and chemically distinct from the widespread propylitic alteration in the area. Mineralization into the wall rock is restricted based on physical and chemical evidence, typically not exceeding 1.5 m laterally. This indicates focused fluid flow, though areas with more intense brecciation can result in greater penetration into the wall rock making wider ore zones.

The mineral assemblages and compositions vary with increasing distance from the deposit, while the modal abundances show a dependence on host rock. Pyrite and chalcopyrite dominate the fissures in the porphyry environment, while galena, sphalerite, and tennantite additionally appear in the epithermal environment. The limestone-hosted fissures have substantially larger amounts of galena and sphalerite (and higher grades of Cu, Au, and Ag when considering a larger fissure sample set). The appearance of both galena and sphalerite—and tennantite to an extent—mark the transition from a porphyry to epithermal environment (in both time and space). This is accompanied by an increased concentration of chalcophile trace elements in sulfides in the fissures. The sulfides have typical chalcophile trace element concentrations, of which tennantite has the highest concentrations. The mineralogical host of Au

could not be determined, although pyrite appears to be the dominant contributor simply due to its overwhelming modal abundance. Significant hosts of Ag include galena and tennantite, while Cu is hosted primarily in chalcopyrite, tennantite, and sphalerite. The trace element analyses of the sulfides presented in this study add to the ever-growing data available that can possibly be used as a vector tool in mineral exploration, while also providing constraints in the development of potential geothermometers based on sulfide composition.

The source of mineralization appears to have been the same mineralizing fluids that produced the main Cu-Mo ore body. This is largely determined by the magmatic signature of the sulfur isotopic composition of pyrite (2.3 to 3.4‰) and systematic appearance of mineral assemblages associated with cooling fluids with increased distance from the center of the deposit. The oxygen isotopes are more difficult to explain because of the elevated $\delta^{18}O$ values (11.5-14.0‰). We propose that the isotope signature is simply the result of pulses of magmatic mineralizing fluids cooling with distance, which would cause higher isotope fractionation. Mixing of the magmatic water with meteoric water would further oxidize and cool the fluids while diluting the ligands and promoting sulfide deposition. The meteoric water could have been enriched in ^{18}O as a result of being heated and convected through the ^{18}O-rich sedimentary rocks following intrusion of magma, though this is not required to explain the high $\delta^{18}O$ values of quartz from the fissures. The timing of fissure mineralization is late-stage: fissure-related alteration overprints all other hydrothermal alteration, fissures cut all igneous units and most faults and joints, and late Au-rich tennantite with high Au-As on pyrite rims suggest an inward movement of a high-sulfidation environment during the collapse of the hydrothermal system.

Fissure ore grades at Bingham improve with distance from the center of the deposit. However, this is accompanied by higher concentrations of problematic elements (As, Bi, Ni, Pb,

Sb, Se, Sn, Te, and Zn), which present challenges to ore processing. The restricted mineralization haloes of the fissures also mean that swarms of fissures are typically required for an ore body of adequate size to be mined by open-pit techniques. Nonetheless, all rock types (limestone, monzonite, and quartzite) can be economic to mine when considering both ore grades and recovery rates.

The mineralized fissures were created sequentially throughout the formation of the deposit (Figs. 15 and 16). Initially NE-trending joints and faults may have formed in the sedimentary host rocks as a result of roof deformation during emplacement of the barren equigranular monzonite intrusion. The NE orientation of the joints was probably controlled by the regional stress-field, which is apparent in the orientation of distal faults and fractures. The later intrusion of the quartz monzonite porphyry, thought to be the main source of mineralization, may have set up the hydrothermal system, dilated these joints, and allowed precipitation of quartz and then pyrite during the early Cu-Au-stage of mineralization in the main ore body. After the latite porphyry and quartz latite porphyry intruded, Pb-Zn-Ag mineralization likely precipitated galena, sphalerite, and pyrite. This was followed by late precipitation of chalcopyrite and tennantite in the fissure veins during the collapse of the hydrothermal system and inward movement of a high-sulfidation epithermal environment.

Base metal veins associated with porphyry deposits are not unique to Bingham, thus the findings of this study can be used to better understand other deposits, improve efficiency in mining, processing, and exploration efforts. Expansion of open pit porphyry copper mines is accompanied by tremendous expense, which can be partly alleviated by exploiting more distal fissure-like structures that can form sizable and economic ore bodies.

REFERENCES

Atkinson, W., and Einaudi, M. T., 1978, Skarn formation and mineralization in the contact
aureole at Carr Fork, Bingham, Utah: Economic Geology, v. 73, p. 1326-1365.

Audétat, A., Heinrich, C. A., and Günther, D., 2000, Causes for large-scale metal zonation
around mineralized plutons: Fluid inclusion LA-ICP-MS evidence from the Mole
Granite, Australia: Economic Geology, v. 95, p. 1563-1581.

Best, M. G., Christiansen, E. H., de Silva, S., and Lipman, P. W., 2016, Slab-rollback ignimbrite
flareups in the southern Great Basin and other Cenozoic American arcs: A distinct style
of arc volcanism: Geosphere, v. 12, p. 1097-1135.

Bortnikov, N. S., Genkin, A. D., Dobrovol'skaya, M. G., Muravitskaya, G. N., and Filimonova,
A. A., 1991, The nature of chalcopyrite inclusions in sphalerite: Exsolution,
coprecipitation, or "disease"?: Economic Geology, v. 86, p. 1070-1082.

Boutwell, J. M., 1905, Economic geology of the Bingham mining district, Utah: US Geological
Survey Professional Paper 38, p. 413.

Bowman, J. R., Parry, W. T., Kropp, W. P., and Kruer, S. A., 1987, Chemical and isotopic
evolution of hydrothermal solutions at Bingham, Utah: Economic Geology, v. 82, p. 395-
428.

Cammans, P. C., 2015, Mechanisms and Timing of Pluton Emplacement in Taranaki Basin, New
Zealand Using Three-Dimensional Seismic Analysis: Unpub. MS thesis, Brigham Young
University, 62 p.

Catchpole, H., Kouzmanov, K., Putlitz, B., Seo, J. H., and Fontboté, L., 2015, Zoned base metal
mineralization in a porphyry system: Origin and evolution of mineralizing fluids in the
Morococha district, Peru: Economic Geology, v. 110, p. 39-71.

Clayton, R. N., and Mayeda, T. K., 1963, The use of bromine pentafluoride in the extraction of

       oxygen from oxides and silicates for isotopic analysis: Geochimica et Cosmochimica

       Acta, v. 27, p. 43-52.

Cook, N., Ciobanu, C., George, L., Zhu, Z.-Y., Wade, B., and Ehrig, K., 2016, Trace element

       analysis of minerals in magmatic-hydrothermal ores by laser ablation inductively-coupled

       plasma mass spectrometry: Approaches and opportunities: Minerals, v. 6, p. 1-34.

Cook, N. J., Ciobanu, C. L., and Mao, J., 2009a, Textural control on gold distribution in As-free

       pyrite from the Dongping, Huangtuliang and Hougou gold deposits, North China Craton

       (Hebei Province, China): Chemical Geology, v. 264, p. 101-121.

Cook, N. J., Ciobanu, C. L., Pring, A., Skinner, W., Shimizu, M., Danyushevsky, L., Saini-

       Eidukat, B., and Melcher, F., 2009b, Trace and minor elements in sphalerite: A LA-

       ICPMS study: Geochimica et Cosmochimica Acta, v. 73, p. 4761-4791.

Cunningham, C. G., Austin, G. W., Naeser, C. W., Rye, R. O., Ballantyne, G. H., Stamm, R. G.,

       and Barker, C. E., 2004, Formation of a paleothermal anomaly and disseminated gold

       deposits associated with the Bingham Canyon porphyry Cu-Au-Mo system, Utah:

       Economic Geology, v. 99, p. 789-806.

Deino, A., and Keith, J. D., 1997, Ages of volcanic and intrusive rocks in the Bingham mining

       district, Utah, Society of Economic Geologists Guidebook Series, 29, p. 91-100.

Dilles, J. H., and Einaudi, M. T., 1992, Wall-rock alteration and hydrothermal flow paths about

       the Ann-Mason porphyry copper deposit, Nevada: A 6-km vertical reconstruction:

       Economic Geology, v. 87, p. 1963-2001.

Dilles, J. H., Solomon, G. C., Taylor, H. P., and Einaudi, M. T., 1992, Oxygen and hydrogen
   isotope characteristics of hydrothermal alteration at the Ann-Mason porphyry copper
   deposit, Yerington, Nevada: Economic Geology, v. 87, p. 44-63.

Dubosq, R., Lawley, C., Rogowitz, A., Schneider, D., and Jackson, S., 2018, Pyrite deformation
   and connections to gold mobility: Insight from micro-structural analysis and trace
   element mapping: Lithos, v. 310, p. 86-104.

Eastoe, C. J., 1983, Sulfur isotope data and the nature of the hydrothermal systems at the
   Panguna and Frieda porphyry copper deposits, Papua New Guinea: Economic Geology,
   v. 78, p. 201-213.

Einaudi, M. T., Hedenquist, J. W., and Inan, E. E., 2003, Sulfidation state of fluids in active and
   extinct hydrothermal systems: Transitions from porphyry to epithermal environments:
   Society of Economic Geologists Special Publication 10, p. 285-314.

Field, C., Zhang, L., Dilles, J., Rye, R. O., and Reed, M., 2005, Sulfur and oxygen isotopic
   record in sulfate and sulfide minerals of early, deep, pre-Main Stage porphyry Cu–Mo
   and late Main Stage base-metal mineral deposits, Butte district, Montana: Chemical
   Geology, v. 215, p. 61-93.

Field, C. W., 1966, Sulfur isotope abundance data, Bingham District, Utah: Economic Geology,
   v. 61, p. 850-871.

Field, C. W., and Moore, W. J., 1971, Sulfur isotope study of the 'B' limestone and Galena
   fissure ore deposits of the US Mine, Bingham mining district, Utah: Economic Geology,
   v. 66, p. 48-62.

Franchini, M., McFarlane, C., Maydagán, L., Reich, M., Lentz, D. R., Meinert, L., and Bouhier,
   V., 2015, Trace metals in pyrite and marcasite from the Agua Rica porphyry-high

sulfidation epithermal deposit, Catamarca, Argentina: Textural features and metal zoning at the porphyry to epithermal transition: Ore Geology Reviews, v. 66, p. 366-387.

George, L., Cook, N., and Ciobanu, C., 2017, Minor and trace elements in natural tetrahedrite-tennantite: Effects on element partitioning among base metal sulphides: Minerals, v. 7, p. 1-25.

George, L., Cook, N. J., Ciobanu, C. L., and Wade, B. P., 2015, Trace and minor elements in galena: A reconnaissance LA-ICP-MS study: American Mineralogist, v. 100, p. 548-569.

George, L. L., Cook, N. J., and Ciobanu, C. L., 2016, Partitioning of trace elements in co-crystallized sphalerite–galena–chalcopyrite hydrothermal ores: Ore Geology Reviews, v. 77, p. 97-116.

George, L. L., Cook, N. J., Crowe, B. B., and Ciobanu, C. L., 2018, Trace elements in hydrothermal chalcopyrite: Mineralogical Magazine, v. 82, p. 59-88.

Grant, J. A., 1986, The isocon diagram: a simple solution to Gresens' equation for metasomatic alteration: Economic Geology, v. 81, p. 1976-1982.

Gruen, G., Heinrich, C. A., and Schroeder, K., 2010, The Bingham Canyon porphyry Cu-Mo-Au deposit. II. Vein geometry and ore shell formation by pressure-driven rock extension: Economic Geology, v. 105, p. 69-90.

Hattori, K. H., and Keith, J. D., 2001, Contribution of mafic melt to porphyry copper mineralization: evidence from Mount Pinatubo, Philippines, and Bingham Canyon, Utah, USA: Mineralium Deposita, v. 36, p. 799-806.

Hezarkhani, A., and Williams-Jones, A. E., 1998, Controls of alteration and mineralization in the Sungun porphyry copper deposit, Iran: Evidence from fluid inclusions and stable isotopes: Economic Geology, v. 93, p. 651-670.

Hildreth, S., Jr., and Hannah, J. L., 1996, Fluid inclusion and sulfur isotope studies of the Tintic

    Mining District, Utah: Implications for targeting fluid sources: Economic Geology, v. 91,

    p. 1270-1281.

James, A., Smith, W., and Welsh, J., 1961, General geology and structure of the Bingham

    district, Utah: Utah Geological Society Guidebook 16, p. 49-71.

Khashgerel, B.-E., Rye, R. O., Hedenquist, J. W., and Kavalieris, I., 2006, Geology and

    reconnaissance stable isotope study of the Oyu Tolgoi porphyry Cu-Au system, South

    Gobi, Mongolia: Economic Geology, v. 101, p. 503-522.

Kloppenburg, A., Grocott, J., and Hutchinson, D., 2010, Structural setting and synplutonic fault

    kinematics of a Cordilleran Cu-Au-Mo porphyry mineralization system, Bingham Mining

    District, Utah: Economic Geology, v. 105, p. 743-761.

Kowallis, B. J., Christiansen, E. H., Blatter, T. K., and Keith, J. D., 1995, Tertiary paleostress

    variation in time and space near the eastern margin of the Basin and Range Province,

    Utah: 2nd International Conference on the Mechanics of Jointed and Faulted Rock,

    Vienna, Austria, April 10-14, 1995, p. 297-302.

Landtwing, M. R., Furrer, C., Redmond, P. B., Pettke, T., Guillong, M., and Heinrich, C. A.,

    2010, The Bingham Canyon porphyry Cu-Mo-Au deposit. III. Zoned copper-gold ore

    deposition by magmatic vapor expansion: Economic Geology, v. 105, p. 91-118.

Landtwing, M. R., Pettke, T., Halter, W. E., Heinrich, C. A., Redmond, P. B., Einaudi, M. T.,

    and Kunze, K., 2005, Copper deposition during quartz dissolution by cooling magmatic–

    hydrothermal fluids: the Bingham porphyry: Earth and Planetary Science Letters, v. 235,

    p. 229-243.

Large, R. R., Danyushevsky, L., Hollit, C., Maslennikov, V., Meffre, S., Gilbert, S., Bull, S., Scott, R., Emsbo, P., and Thomas, H., 2009, Gold and trace element zonation in pyrite using a laser imaging technique: Implications for the timing of gold in orogenic and Carlin-style sediment-hosted deposits: Economic Geology, v. 104, p. 635-668.

Large, S. J. E., 2018, The magmatic to hydrothermal evolution of porphyry Cu-Au deposits: A zircon perspective: Unpub. PhD thesis, Eidgenössische Technische Hochschule Zürich, 133 p.

Li, Y., Li, X.-H., Selby, D., and Li, J.-W., 2017, Pulsed magmatic fluid release for the formation of porphyry deposits: Tracing fluid evolution in absolute time from the Tibetan Qulong Cu-Mo deposit: Geology, v. 46, p. 7-10.

Mao, J., Zhang, J., Pirajno, F., Ishiyama, D., Su, H., Guo, C., and Chen, Y., 2011, Porphyry Cu–Au–Mo–epithermal Ag–Pb–Zn–distal hydrothermal Au deposits in the Dexing area, Jiangxi province, East China—A linked ore system: Ore Geology Reviews, v. 43, p. 203-216.

Maughan, D. T., Keith, J. D., Christiansen, E. H., Pulsipher, T., Hattori, K., and Evans, N. J., 2002, Contributions from mafic alkaline magmas to the Bingham porphyry Cu–Au–Mo deposit, Utah, USA: Mineralium Deposita, v. 37, p. 14-37.

Maydagán, L., Franchini, M., Lentz, D., Pons, J., and McFarlane, C., 2013, Sulfide composition and isotopic signature of the Altar Cu-Au deposit, Argentina: Constraints on the evolution of the porphyry-epithermal system: The Canadian Mineralogist, v. 51, p. 813-840.

McDonough, W. F., and Sun, S. s., 1995, The composition of the Earth: Chemical Geology, v. 120, p. 223-253.

McKean, A. P., Kowallis, B. J., and Christiansen, E. H., 2011, Kinematic analysis of northeast-trending faults of the Allens Ranch 7.5' quadrangle, Utah County, Utah, *in* Sprinkel, D. A., Yonkee, W. A., and Chidsey, T. C., Jr, eds., Sevier thrust belt: northern and central Utah and adjacent areas: Salt Lake City, Utah Geological Association Publication 40, p. 89-116.

Miller, J. W., and Craig, J. R., 1983, Tetrahedrite-tennantite series compositional variations in the Cofer Deposit, Mineral District, Virginia: American Mineralogist, v. 68, p. 227-234.

Mirnejad, H., Mathur, R., Hassanzadeh, J., Shafie, B., and Nourali, S., 2013, Linking Cu mineralization to host porphyry emplacement: Re-Os ages of molybdenites versus U-Pb ages of zircons and sulfur isotope compositions of pyrite and chalcopyrite from the Iju and Sarkuh porphyry deposits in southeast Iran: Economic Geology, v. 108, p. 861-870.

Muller, O. H., and Pollard, D. D., 1977, The stress state near Spanish Peaks, Colorado determined from a dike pattern: Pure and Applied Geophysics, v. 115, p. 69-86.

Muntean, J. L., and Einaudi, M. T., 2001, Porphyry-epithermal transition: Maricunga belt, northern Chile: Economic Geology, v. 96, p. 743-772.

Murowchick, J. B., and Barnes, H. L., 1986, Marcasite precipitation from hydrothermal solutions: Geochimica et Cosmochimica Acta, v. 50, p. 2615-2629.

Pačevski, A., Libowitzky, E., Živković, P., Cvetković, L., and Dimitrijević, R., 2008, Copper-bearing pyrite from the Čoka Marin polymetallic deposit, Serbia: Mineral inclusions or true solid-solution?: The Canadian Mineralogist, v. 46, p. 249-261.

Palenik, C. S., Utsunomiya, S., Reich, M., Kesler, S. E., Wang, L., and Ewing, R. C., 2004, "Invisible" gold revealed: Direct imaging of gold nanoparticles in a Carlin-type deposit: American Mineralogist, v. 89, p. 1359-1366.

Palero-Fernández, F. J., and Martín-Izard, A., 2005, Trace element contents in galena and

      sphalerite from ore deposits of the Alcudia Valley mineral field (Eastern Sierra Morena,

      Spain): Journal of Geochemical Exploration, v. 86, p. 1-25.

Paton, C., Hellstrom, J., Paul, B., Woodhead, J., and Hergt, J., 2011, Iolite: Freeware for the

      visualisation and processing of mass spectrometric data: Journal of Analytical Atomic

      Spectrometry, v. 26, p. 2508-2518.

Porter, J. P., Schroeder, K., and Austin, G., 2012, Geology of the Bingham Canyon porphyry

      Cu-Mo-Au deposit, Utah: Society of Economic Geologists Special Publication 16, p.

      127-146.

Presnell, R., 1997, Structural controls on the plutonism and metallogeny in the Wasatch and

      Oquirrh Mountains, Utah: Society of Economic Geolgists Guidebook Series 29, p. 1-14.

Redmond, P. B., and Einaudi, M. T., 2010, The Bingham Canyon porphyry Cu-Mo-Au deposit.

      I. Sequence of intrusions, vein formation, and sulfide deposition: Economic Geology, v.

      105, p. 43-68.

Reich, M., Deditius, A., Chryssoulis, S., Li, J.-W., Ma, C.-Q., Parada, M. A., Barra, F., and

      Mittermayr, F., 2013, Pyrite as a record of hydrothermal fluid evolution in a porphyry

      copper system: A SIMS/EMPA trace element study: Geochimica et Cosmochimica Acta,

      v. 104, p. 42-62.

Reich, M., Kesler, S. E., Utsunomiya, S., Palenik, C. S., Chryssoulis, S. L., and Ewing, R. C.,

      2005, Solubility of gold in arsenian pyrite: Geochimica et Cosmochimica Acta, v. 69, p.

      2781-2796.

Ren, X., Kowallis, B. J., and Best, M. G., 1989, Paleostress history of the Basin and Range province in western Utah and eastern Nevada from healed microfracture orientations in granites: Geology, v. 17, p. 487-490.

Rottier, B., Kouzmanov, K., Wälle, M., Bendezú, R., and Fontboté, L., 2016, Sulfide replacement processes revealed by textural and LA-ICP-MS trace element analyses: example from the early mineralization stages at Cerro de Pasco, Peru: Economic Geology, v. 111, p. 1347-1367.

Rye, R. O., and Ohmoto, H., 1974, Sulfur and carbon isotopes and ore genesis: A review: Economic Geology, v. 69, p. 826-842.

Sack, R. O., and Loucks, R. R., 1985, Thermodynamic properties of tetrahedrite-tennantite: constraints on the interdependence of the Ag$\rightleftharpoons$ Cu, Fe$\rightleftharpoons$ Zn, Cu$\rightleftharpoons$ Fe, and As$\rightleftharpoons$ Sb exchange reactions: American Mineralogist, v. 70, p. 1270-1289.

Seedorf, E., 2005, Porphyry deposits: Characteristics and origin of hypogene features: Economic Geology, v. 100, p. 251-298.

Seo, J. H., Guillong, M., and Heinrich, C. A., 2012, Separation of molybdenum and copper in porphyry deposits: The roles of sulfur, redox, and pH in ore mineral deposition at Bingham Canyon: Economic Geology, v. 107, p. 333-356.

Sharp, Z. D., Gibbons, J. A., Maltsev, O., Atudorei, V., Pack, A., Sengupta, S., Shock, E. L., and Knauth, L. P., 2016, A calibration of the triple oxygen isotope fractionation in the SiO_2–H_2O system and applications to natural samples: Geochimica et Cosmochimica Acta, v. 186, p. 105-119.

Sheppard, S. M. F., and Gustafson, L. B., 1976, Oxygen and hydrogen isotopes in the porphyry copper deposit at El Salvador, Chile: Economic Geology, v. 71, p. 1549-1559.

Sillitoe, R. H., 2010, Porphyry copper systems: Economic geology, v. 105, p. 3-41.

Spry, P. G., Paredes, M. M., Foster, F., Truckle, J. S., and Chadwick, T. H., 1996, Evidence for a genetic link between gold-silver telluride and porphyry molybdenum mineralization at the Golden Sunlight Deposit, Whitehall, Montana: Fluid inclusion and stable isotope studies: Economic Geology, v. 91, p. 507-526.

Steinberger, I., Hinks, D., Driesner, T., and Heinrich, C. A., 2013, Source plutons driving porphyry copper ore formation: Combining geomagnetic data, thermal constraints, and chemical mass balance to quantify the magma chamber beneath the Bingham Canyon deposit: Economic Geology, v. 108, p. 605-624.

Sykora, S., Cooke, D. R., Meffre, S., Stephanov, A. S., Gardner, K., Scott, R., Selley, D., and Harris, A. C., 2018, Evolution of pyrite trace element compositions from porphyry-style and epithermal conditions at the Lihir gold deposit: Implications for ore genesis and mineral processing: Economic Geology, v. 113, p. 193-208.

Tanner, D., Henley, R. W., Mavrogenes, J. A., and Holden, P., 2016, Sulfur isotope and trace element systematics of zoned pyrite crystals from the El Indio Au–Cu–Ag deposit, Chile: Contributions to Mineralogy and Petrology, v. 171, p. 33.

Tardani, D., Reich, M., Deditius, A. P., Chryssoulis, S., Sánchez-Alfaro, P., Wrage, J., and Roberts, M. P., 2017, Copper–arsenic decoupling in an active geothermal system: A link between pyrite and fluid composition: Geochimica et Cosmochimica Acta, v. 204, p. 179-204.

Taylor, H., 1974, The application of oxygen and hydrogen isotope studies to problems of hydrothermal alteration and ore deposition: Economic geology, v. 69, p. 843-883.

Wark, D. A., and Watson, E. B., 2006, TitaniQ: a titanium-in-quartz geothermometer: Contributions to Mineralogy and Petrology, v. 152, p. 743-754.

White, D. E., 1974, Diverse origins of hydrothermal ore fluids: Economic Geology, v. 69, p. 954-973.

Whitmeyer, S. J., and Karlstrom, K. E., 2007, Tectonic model for the Proterozoic growth of North America: Geosphere, v. 3, p. 220-259.

Wilson, S. A., Ridley, W. I., and Koenig, A. E., 2002, Development of sulfide calibration standards for the laser ablation inductively-coupled plasma mass spectrometry technique: Journal of Analytical Atomic Spectrometry, v. 17, p. 406-409.

Wu, Y.-F., Li, J.-W., Evans, K., Koenig, A. E., Li, Z.-K., O'Brien, H., Lahaye, Y., Rempel, K., Hu, S.-Y., Zhang, Z.-P., and Yu, J.-P., 2018, Ore-forming processes of the Daqiao epizonal orogenic gold deposit, west Qinling orogen, China: Constraints from textures, trace elements, and sulfur isotopes of pyrite and marcasite, and raman spectroscopy of carbonaceous material: Economic Geology, v. 113, p. 1093-1132.

Yonkee, W. A., and Weil, A. B., 2015, Tectonic evolution of the Sevier and Laramide belts within the North American Cordillera orogenic system: Earth-Science Reviews, v. 150, p. 531-593.

Zhang, G., Xue, C., Chi, G., Liu, J., Zhao, X., Zu, B., and Zhao, Y., 2017, Multiple-stage mineralization in the Sawayaerdun orogenic gold deposit, western Tianshan, Xinjiang: Constraints from paragenesis, EMPA analyses, Re–Os dating of pyrite (arsenopyrite) and U–Pb dating of zircon from the host rocks: Ore Geology Reviews, v. 81, p. 326-341.

Zhang, L., 2000, Stable isotope investigation of a hydrothermal alteration system: Butte porphyry copper deposit: Unpub. PhD thesis, Oregon State University, 182 p.